

Lattice dynamics of *Pnma* Sn(S_{1-x}Se_x) solid solutions: energetics, phonon spectra and thermal transport

Jonathan M. Skelton^{1*}

¹ *Department of Chemistry, University of Manchester, Oxford Road, Manchester M13 9PL, UK*

* Corresponding author - e-mail jonathan.skelton@manchester.ac.uk

Abstract

Alloying is widely used as a means to fine-tune the properties of thermoelectric materials by reducing the lattice thermal conductivity. However, the effects of compositional variation on the lattice dynamics of alloy systems are not well understood, due in part to the difficulty of building realistic first-principles models of structurally-complex solid solutions. This work builds on our previous study of Sn_n(S_{1-x}Se_x)_m solid solutions [Gunn *et al.*, *Chem. Mater.* **31**, 10, 3672, 2019] to explore the lattice dynamics of the *Pnma* Sn(S_{1-x}Se_x) system, which has been widely studied for potential thermoelectric applications. We find that the vibrational internal energy and entropy have a large quantitative impact on the mixing free energy and are likely to be particularly important in alloy systems with competing phases. The thermodynamically-averaged phonon dispersions and density of states curves show that alloying preserves the structure of the low-frequency bands of modes associated with the Sn sublattice but broadens the high-frequency chalcogen bands into a near-continuous spectrum at the 50/50 mixed composition. This results in a general reduction in the phonon mode group velocities and an increase in the number of energy-conserving scattering channels for heat-carrying low-frequency modes, which is consistent with the decrease in thermal conductivity observed in experimental measurements. Finally, we discuss some of the limitations of our first-principles modelling approach and propose methods to address these in future studies.

Introduction

Around two thirds of the energy used globally is wasted as low-grade heat from sources including industry, refrigeration and transportation[1]. Thermoelectric (TE) power provides a means to recover electrical energy from temperature gradients and thereby enable significant efficiency gains in these energy-intensive processes, making it an important complement to primary renewable energy sources such as photovoltaics (PV). In particular, in the drive to meet ambitious climate change targets, emissions from internal combustion engines are becoming a huge area of concern, and employing thermoelectric generation as part of a mild hybrid powertrain could provide an interim solution while electric vehicle technology and infrastructure matures to allow for more widespread adoption.

The efficiency of a thermoelectric material is commonly expressed by the dimensionless figure of merit ZT [2]:

$$ZT = \frac{S^2 \sigma T}{\kappa_{\text{latt}} + \kappa_{\text{el}}} \quad (1)$$

The Seebeck coefficient S , electrical conductivity σ and electronic thermal conductivity κ_{el} are interdependent such that the balance of a high power factor $S^2 \sigma$ and low κ_{el} is generally found in doped semiconductors. At low to moderate temperatures, the lattice thermal conductivity κ_{latt} makes the most significant contribution to the denominator, and thus minimising κ_{latt} has proven to be a facile means of improving TE performance. In some cases the electronic and thermal transport can be almost completely decoupled[1], as in the “phonon glass, electron crystal” concept[3]. All four parameters in Eq. 1 are implicit functions of temperature, requiring that materials are either optimised to produce a high peak ZT at a target operating temperature range or tuned to display a high ZT across a wide range of temperatures.

Current flagship TE materials include PbTe, SnSe and Bi₂Te₃, all three of which display favourable electrical properties and intrinsically low thermal conductivity due to a combination of heavy elements and strongly anharmonic lattice dynamics[4–6]. However, PbTe and Bi₂Te₃ are not suitable for widespread adoption due to the low abundance of Te, and there are also concerns with SnSe due to the environmental toxicity of Se. There has therefore been significant effort devoted to alternative systems including the more earth-abundant SnS[2] and metal oxides[7–10].

Alloying is commonly used as a means to enhance thermoelectric performance, as a suitable choice of components can maintain or improve a favourable electronic structure while reducing κ_{latt} by introducing variation in atomic masses and chemical bond strength to promote stronger phonon scattering[11]. Pb(S,Se,Te), Sn(S,Se) and (Bi,Sb)₂(Se,Te)₃ alloys have all been studied as thermoelectrics and the alloying shown to improve ZT [12–17]. Due to the record-breaking high-temperature ZT of SnS, the Te-free Sn(S,Se) alloys are of particular interest, and experimental studies have demonstrated a reduction in the thermal conductivity of mixed compositions[12,14].

Thermoelectricity is unique in that all four of the terms in the figure of merit ZT are amenable to calculation using first-principles electronic-structure methods such as density-functional theory[18]. There have been a number of theoretical studies on existing and potential new single-component bulk thermoelectrics[6,19–23], and there have recently been efforts to use high-throughput modelling to screen large numbers of compounds in a bid to identify new candidate thermoelectrics[24,25].

Studying multicomponent alloy systems with first-principles methods is challenging, however, as building a realistic model requires calculations on a large number of configurations that for complex systems with low-symmetry unit cells can easily approach the cost of a screening study[26]. Ektarawong and Alling used a first-principles cluster expansion method to study the *Pnma* Sn(S_{1-x}Se_x) system and confirmed the stability of the mixed phases at finite temperature[27]. We recently carried out a study of four Sn_n(S_{1-x}Se_x)_m alloys[26], including the *Pnma* and rocksalt monosulphides, by performing first-principles calculations on the full sets of symmetry-inequivalent structures formed by substituting chalcogen atoms in small supercells of the parent structures[28]. In this study we also confirmed the stability of the mixed *Pnma* Sn(S_{1-x}Se_x) alloys and further predicted the effect of alloying on the structural, electrical and optical properties[26].

While many large-scale modelling studies make use of (semi-)local DFT methods to evaluate and compare energetics and electrical properties[29–32], modelling lattice dynamics and in particular thermal transport can be much more resource intensive, and there are thus comparatively fewer examples of screening studies focussing on these properties[33]. As a result, despite the widespread use of alloying to tune the performance of thermoelectric materials, there has been little theoretical investigation into how composition affects the dynamics and related properties. In this work, the model developed in Ref. [26] is extended to include explicit evaluation of the lattice dynamics of the *Pnma* Sn(S_{1-x}Se_x) solid solution. We quantify the effect of the phonon free energy on the mixing energetics, establish the effect of alloying on the phonon spectrum and frequency dispersion, and explore some of the implications for the thermal transport. Finally, we discuss the broader applicability of this modelling technique and possible future enhancements.

Computational modelling

The starting point for our calculations was the set of optimised structures in the *Pnma* Sn(S_{1-x}Se_x) solid solution model from our previous study[26]. In our previous work, the Transformer code[34] was used to enumerate the symmetry-independent structures formed by successively substituting the chalcogen atoms in a 32-atom 2×1×2 expansion of the *Pnma* SnS/SnSe structure, yielding a total of 2,446 unique structures across seventeen compositions from $x_{\text{Se}} = 0$ (SnS) to $x_{\text{Se}} = 1$ (SnSe). In the present study, lattice dynamics calculations were performed on a subset of 1,294 structures in nine compositions, *viz.* $x_{\text{Se}} = 0, 0.125, 0.25, 0.375, 0.5, 0.625, 0.75, 0.875$ and 1, using the finite-displacement method implemented in the Phonopy package.[35]

The accuracy of the phonon frequencies obtained using the finite-displacement method depends on the range of the real-space interatomic force constants (IFCs) evaluated with the chosen supercell expansion. Taking into account the symmetry of individual structures in the alloy model, where present, between 8 and 192 accurate calculations were required to evaluate the IFCs for each structure, generally representing a considerably larger computational workload than the initial geometry optimisations. For this reason, the force constants were calculated using the 32-atom alloy supercell structures, *i.e.* without further expansion.

Phonon density of states (DoS) and atom-projected DoS (PDoS) curves were evaluated using Fourier interpolation to obtain frequencies on uniform Γ -centered grids of phonon wavevectors with 24×16×24 subdivisions, with a Gaussian smearing of width $\sigma = 0.032$ THz (FWHM ~ 2.5 cm⁻¹). The vibrational contributions to the thermodynamic free energy were evaluated using denser sampling meshes with 36×24×36 subdivisions. Phonon band dispersions were evaluated using the band-unfolding scheme implemented in Phonopy[36] to project the vibrational modes calculated for the alloy supercells back onto the parent *Pnma* structure. The dispersion curves were evaluated across a series of segments passing through all the high-symmetry wavevectors in the *Pnma* Brillouin zone. Calculations of the lattice thermal conductivity of the SnS and SnSe endpoints, and evaluation of the two-phonon joint density of states of the alloy models, were performed using the Phono3py package.[37]

All calculations were performed using pseudopotential plane-wave density-functional theory (DFT) as implemented in the Vienna *Ab initio* Simulation Package (VASP) code[38]. As in our previous study[26], a plane-wave cutoff of 600 eV was employed alongside Monkhorst-Pack k -point sampling grids[39] with $4 \times 4 \times 4$ subdivisions. The PBEsol exchange-correlation functional with the DFT-D3 dispersion correction was used with projector augmented-wave (PAW) pseudopotentials[40,41] including the Sn 5s, 5p and 4d and the outermost 3d/3p and 4s/4p electrons on S and Se in the valence shell. The precision of the charge-density grids was set automatically to avoid aliasing errors, and a support grid with $8 \times$ as many points was used to evaluate the forces. The PAW projection was performed in reciprocal space and nonspherical contributions to the gradient corrections inside the PAW spheres were accounted for.

Results and Discussion

a. Mixing thermodynamics

The solid solution model for a given composition x_{Se} comprises a set of N optimised structures with total energy E_n and degeneracy g_n , which are used to form the thermodynamic partition function at a temperature T , $Z(x_{\text{Se}}, T)$, according to[28]:

$$Z(x_{\text{Se}}, T) = \sum_{n=1}^N g_n \exp(-E_n/k_B T) \quad (2)$$

where k_B is the Boltzmann constant. $Z(x_{\text{Se}}, T)$ is then used to obtain the constant-volume (Helmholtz) free energy $A = U - TS$ from the bridge relation:

$$A(x_{\text{Se}}, T) = -k_B T \ln Z(x_{\text{Se}}, T) \quad (3)$$

From $A(x_{\text{Se}}, T)$, the free energy of mixing $A_{\text{mix}}(x_{\text{Se}}, T)$ can be obtained as:

$$A_{\text{mix}}(x_{\text{Se}}, T) = A(x_{\text{Se}}, T) - [(1 - x_{\text{Se}})A(x_{\text{Se}} = 0, T) + x_{\text{Se}}A(x_{\text{Se}} = 1, T)] \quad (4)$$

where $A(x_{\text{Se}} = 0, T)$ and $A(x_{\text{Se}} = 1, T)$ are the free energies of the SnS and SnSe endmembers respectively, which, since $g_n = 1$, are simply equal to the corresponding E_n .

For a given composition and temperature the occurrence probability of individual structures P_n in the model are calculated from the partition function as:

$$P_n(T) = \frac{1}{Z(T)} g_n \exp(-E_n/k_B T) \quad (5)$$

The P_n can then be used to calculate the thermodynamic average \bar{X} of a general property X using:

$$\bar{X}(T) = \sum_{n=1}^N P_n(T) X_n \quad (6)$$

where X_n are the properties of the individual structures in the model.

This model can be improved upon by using the phonon frequencies obtained from the lattice-dynamics calculations to calculate for each structure the temperature-dependent Helmholtz energy A_n including contributions from vibrations:

$$A_n(T) = E_n + A_n^{\text{vib}} = E_n + U_n^{\text{vib}}(T) - TS_n^{\text{vib}}(T) \quad (7)$$

where A_n^{vib} is the vibrational Helmholtz energy and U_n^{vib} and S_n^{vib} are the vibrational internal energy and entropy. The superscript vib is used for clarity to explicitly identify quantities calculated based on the lattice dynamics. As for the free energy of the solid solution, $A_n^{\text{vib}}(T)$ is calculable from the vibrational partition function $Z_n^{\text{vib}}(T)$ using the bridge relation:

$$Z_n^{\text{vib}}(T) = \prod_{\mathbf{q}v} \frac{\exp(-\hbar\omega_{\mathbf{q}v}/2k_B T)}{1 - \exp(-\hbar\omega_{\mathbf{q}v}/k_B T)} \quad (8)$$

$$\begin{aligned} A_n^{\text{vib}}(T) &= -\frac{1}{N} k_B T \ln Z_n^{\text{vib}}(T) \\ &= \frac{1}{N} \left\{ \frac{1}{2} \sum_{\mathbf{q}v} \hbar\omega_{\mathbf{q}v} + k_B T \sum_{\mathbf{q}v} \ln[1 - \exp(-\hbar\omega_{\mathbf{q}v}/k_B T)] \right\} \end{aligned} \quad (9)$$

Here the phonon frequencies ω are indexed by a phonon wavevector \mathbf{q} and band index v and \hbar is the reduced Planck constant. The product in Eq. 8 runs over all bands on a grid of N wavevectors sampling the phonon Brillouin zone, which appears as a normalisation constant in Eq. 9. The expansion in Eq. 9 shows that A_n^{vib} is a sum of the harmonic zero-point energies $\frac{1}{2} \hbar\omega_{\mathbf{q}v}$ and a temperature-dependent term from the population of higher mode energy levels at finite temperature.

We note that this model assumes the distribution of the different supercell configurations is in thermodynamic equilibrium at the formation temperature T_F [28], and that the chosen alloy supercell is sufficient to sample the range of local configurations that may be present. In real alloy systems, there may be medium- or long-range deviations in local structure and/or composition that are not probed by this method, for example due to the flexible oxidation state and lone-pair activity of Sn[42].

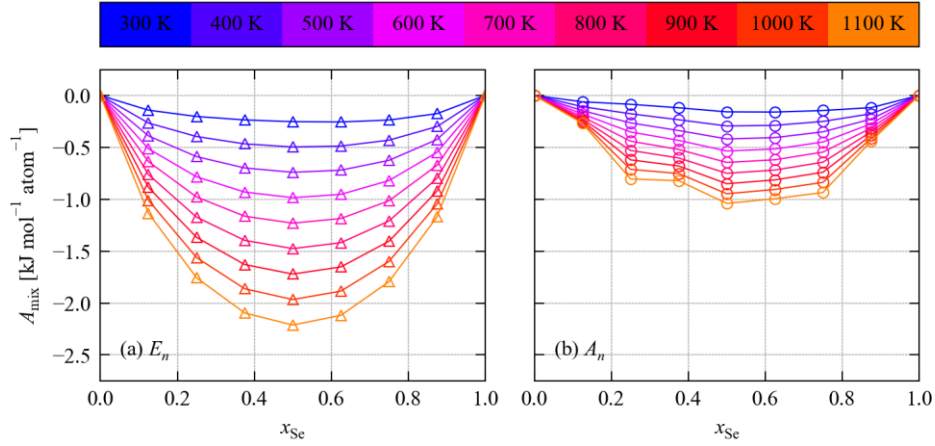


Figure 1 Calculated mixing free energies A_{mix} of *Pnma* $\text{Sn}(\text{S}_{1-x}\text{Se}_x)$ solid solutions as a function of Se fraction x_{Se} , obtained using the lattice energies E_n (a) and the Helmholtz free energies A_n (b) including contributions from the lattice dynamics. Each plot shows $A_{\text{mix}}(x_{\text{Se}})$ for a range of alloy formation temperatures T_F from 300 - 1100 K, which are denoted by line colours from blue (low T_F) to orange (high T_F).

By substituting the E_n in Eq. 2 with A_n (Eq. 7), we can build the partition function for the solid solution and evaluate the mixing free energies including the effect of the lattice dynamics (Fig. 1). Interestingly, we find that including the vibrational free energy terms destabilises the solid solution, decreasing A_{mix} for the 50/50 composition ($x_{\text{Se}} = 0.5$) by a factor of two from -1.72 to -0.85 kJ mol^{-1} per atom at 900 K compared to using the lattice energies. This difference corresponds to $\sim 0.1 \times k_B T$, which is in the typical range of vibrational entropy differences observed by van de Walle and Ceder[43].

For an ideal solid solution, the mixing is purely entropic and the A_{mix} profile would be symmetric with a minimum at $x_{\text{Se}} = 0.5$. The A_{mix} profiles obtained using the E_n show near-ideal behaviour, with the mixing energies of the $x_{\text{Se}} = 0.25$ and $x_{\text{Se}} = 0.75$ compositions differing by 0.04 kJ mol^{-1} atom $^{-1}$ at 900 K. However, a much larger difference of 0.12 kJ mol^{-1} atom $^{-1}$ is obtained when including the free energy, indicating a larger deviation from ideality, which is clearly evident when comparing the two sets of mixing profiles in Fig. 1.

Of particular note are the large deviations from the general trend in Fig. 1a at $x_{\text{Se}} = 0.125$ and 0.375 , the reasons for which are not clear. One possible explanation is that the 32-atom supercell does not adequately capture the full range of local structures present in the bulk alloy, although in our previous study we found that this was at least sufficient to converge the mixing energies calculated from the E_n [26]. Another possibility is that the deviation is an artefact of the limited real-space range of the calculated force constants and its impact on the interpolation of the phonon frequencies to a dense grid of wavevectors to evaluate A_n^{vib} . Although we would naively expect a similar level of accuracy across the nine compositions, we found that the proportion of imaginary frequencies in the wavevector sampling meshes - which are excluded from the partition function in Eq. 8 - ranged from 2.06 ± 0.91 % for the $x_{\text{Se}} = 0.875$ composition to 2.81 ± 0.6 % for $x_{\text{Se}} = 0.375$, so this is a possibility. As an additional test we also recalculated the mixing energy based on the A_n^{vib} obtained with a denser sampling mesh with $54 \times 36 \times 54$ subdivisions and obtained quantitatively similar results (Fig. S1), with a maximum difference of 14 μeV in the absolute free energy per atom across the nine compositions.

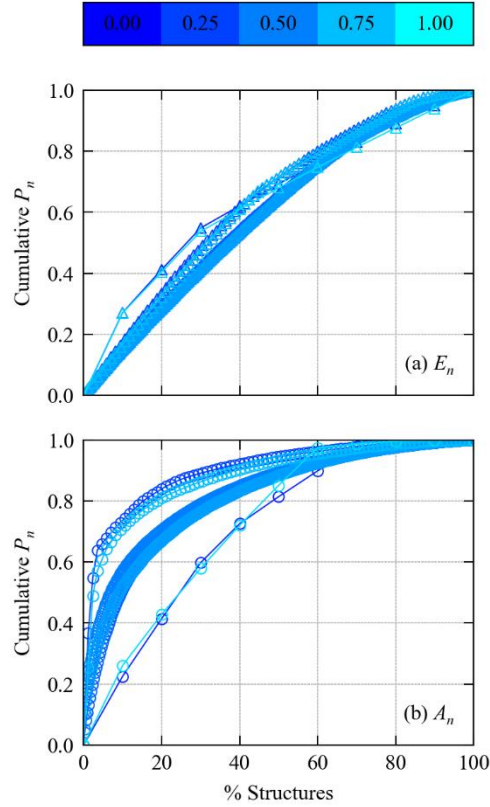


Figure 2 Cumulative occurrence probability P_n as a function of the percentage of structures in the solid solution models with compositions ranging from $x_{\text{Se}} = 0.125$ to 0.875 , calculated using the lattice energies E_n (a) and the free energies A_n (b).

In both cases, the mixing is still energetically favoured at all compositions and the qualitative stability of the alloy is thus unaffected. However, the substantial difference in the mixing energy may be important in systems with competing phases. In our previous work[26,42], we predicted based on lattice energies that the energy difference between competing *Pnma* and rocksalt $\text{Sn}(\text{S}_{1-x}\text{Se}_x)$ monochalcogenide solid solutions varies from 10.5 and 2.6 kJ mol^{-1} per F.U. between the SnS and SnSe endpoints[26]. We also found that the vibrational free energy stabilises the rocksalt phase of SnS relative to the *Pnma* phase at higher temperatures, reducing the energy difference to 4.5 kJ mol^{-1} per F.U. at 900 K [42]. It is therefore conceivable that differences in the free energy may bring the rocksalt phase closer to the convex hull at Se-rich compositions. To test this would require an additional set of lattice dynamics calculations on the rocksalt solid solution models, which we have not attempted here.

Including the vibrational free energy in the partition function also leads to a marked change in the distribution of the occurrence probabilities of individual structures. For the 50/50 composition ($x_{\text{Se}} = 0.5$) and a formation temperature T_F of 900 K , the P_n calculated using the lattice energies range from 8.8×10^{-5} to 4.2×10^{-3} , whereas including the effect of lattice dynamics produces a significantly wider spread of $2.3 \times 10^{-5} - 5.2 \times 10^{-2}$. As shown in Fig. 2, the discrepancy is such that 20% of structures with the highest P_n account for $> 70 \%$ of the partition function formed using the free energies, compared to just under 30% with the lattice energies.

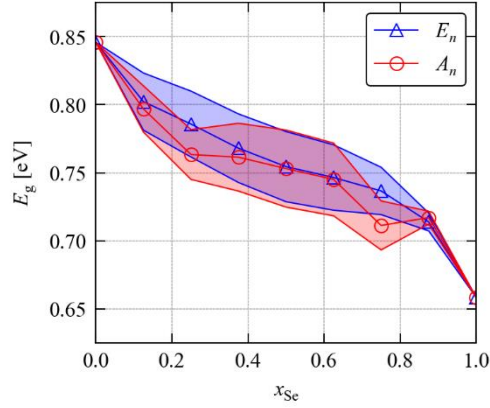


Figure 3 Composition dependence of the electronic bandgap E_g calculated using occurrence probabilities P_n based on the lattice energies E_n (blue triangles) and the Helmholtz energies A_n (red circles). The markers show the calculated averages and the shaded regions show \pm one weighted standard deviation.

The vibrational free energy is derived from the phonon frequencies, which in this system are much more sensitive to the structure than the lattice energy. Again taking the $x_{\text{Se}} = 0.5$ model as an example, the largest difference in E_n between two structures is $3.8 \text{ meV atom}^{-1}$ ($0.36 \text{ kJ mol}^{-1} \text{ atom}^{-1}$), whereas the difference in the zero point energies is $0.06 \text{ kJ mol}^{-1} \text{ atom}^{-1}$ and the difference in A_n^{vib} at 900 K is $2.06 \text{ kJ mol}^{-1} \text{ atom}^{-1}$. Given the number of examples in the literature showing that differences in vibrational free energy - in particular the vibrational entropy - are a key driver of temperature-induced phase transitions[42,44–46] and are important in the determining the stability of alloy systems[43,47,48] - this finding is not surprising, but is nonetheless noteworthy.

In principle, the large change in P_n may lead to a significant change in the averaged properties, although this is likely to be mitigated if the variation in properties among the structures is small. To test this, we took the electronic bandgaps of the *Pnma* structures obtained in our previous study and calculated the averaged bandgap \bar{E}_g as a function of composition using the 900 K occurrence probabilities calculated using the E_n and A_n (Eq. 6, Fig. 3). The two sets of calculated bandgaps for the 50/50 composition differ by only $\sim 1.5 \text{ meV}$, and including the vibrational free energy reduces the averaged bandgaps of the $x_{\text{Se}} = 0.25$ and $x_{\text{Se}} = 0.75$ compositions by 2.8 and 3.4 %, respectively, from 0.79 and 0.74 eV to 0.76 and 0.71 eV. These reductions may be compared to the range of E_g of the individual structures in the three compositions, which are 111, 212 and 80 meV. The weighted standard deviations are also largely unchanged, with the largest difference being a decrease of 5.9 meV for the $x_{\text{Se}} = 0.25$ composition. Our calculations thus suggest that the differences in the P_n do not have a significant impact on the predicted electrical properties of the *Pnma* $\text{Sn}(\text{S}_{1-x}\text{Se}_x)$ alloy.

Finally, we note that in this analysis we have used the Helmholtz rather than the Gibbs free energy $G(x_{\text{Se}}, T)$ as in our previous study. In the absence of contributions to the free energy from the lattice dynamics, the effect of finite pressure can be modelled by replacing the internal energies E_n with the enthalpies $H_n = E_n + pV_n$ [49]. This may be done approximately by adding a correction pV_n to each E_n or by relaxing the structures under applied pressure to evaluate the H_n explicitly. However, thermal expansion at finite temperature has a considerable effect on the phonon spectra and the vibrational contributions to the free energy, which should be accounted for by calculating G_n for each structure within the quasi-harmonic approximation (QHA)[35]. However, to do so for all of the structures in the solid solution model would require an order of magnitude more calculations and is therefore not feasible using first-principles techniques.

b. Phonon spectra

For a given composition and formation temperature T_F , a thermodynamically averaged phonon density of states $g(\nu)$ (DoS) can be obtained by summing the DoS curves of individual structures weighted by the corresponding occurrence probabilities $P_n(T_F)$ (Eq. 5/Eq. 6). Obtaining an averaged phonon dispersion is more involved, as the vibrational modes calculated in the alloy supercells must first be “unfolded” onto the parent structure. In the present study we employed the method proposed by Allen *et al.*[36], which is implemented in recent versions of the Phonopy lattice-dynamics code[35] and accessible through the Python API. Reference structures for the unfolding were generated for each composition by linear interpolation of the lattice vectors and atomic positions between the SnS and SnSe structures.

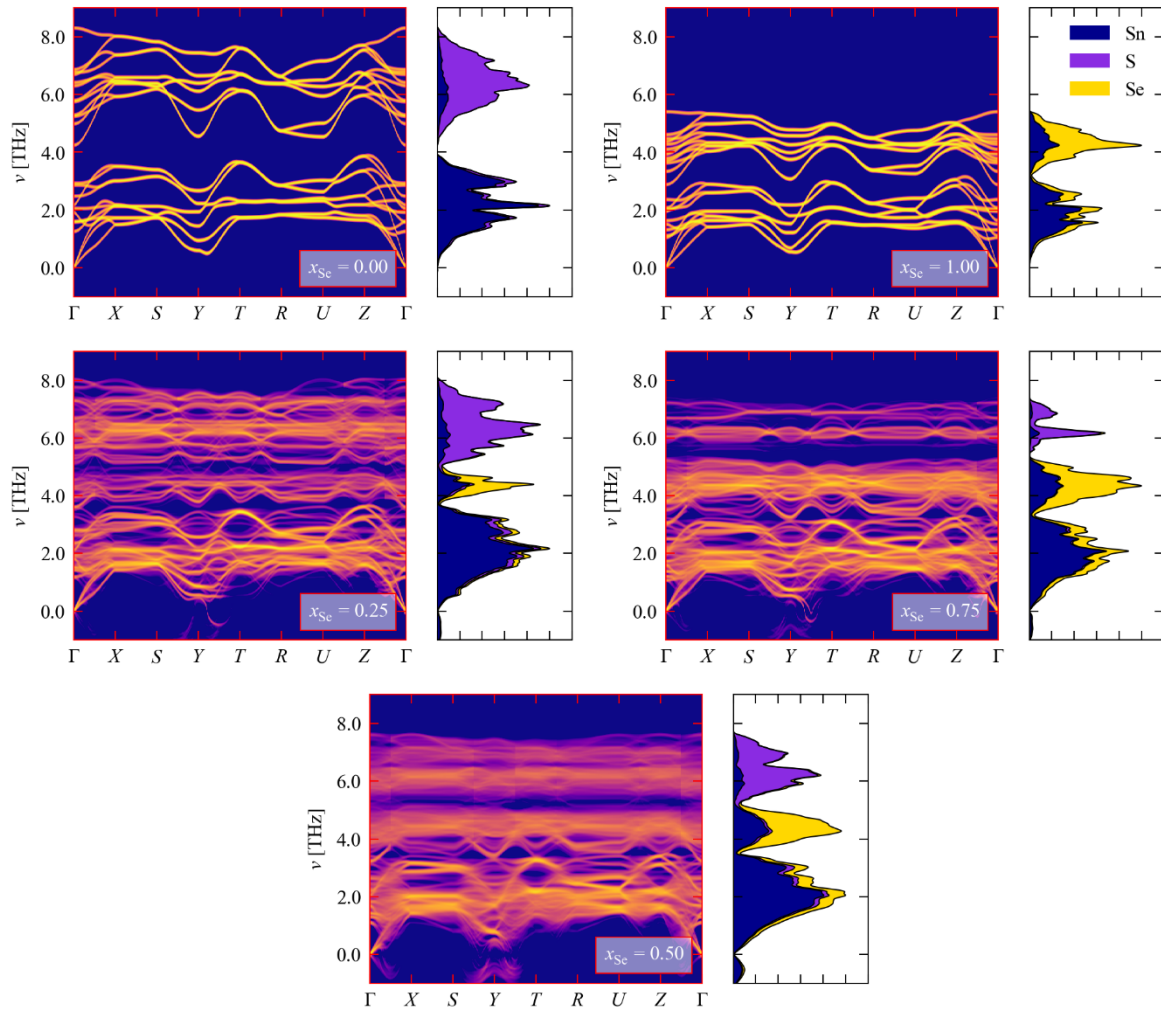


Figure 4 Phonon spectra of $Pnma$ $\text{Sn}(\text{S}_{1-x}\text{Se}_x)$ solid solutions with composition $x_{\text{Se}} = 0, 0.25, 0.5, 0.75$ and 1. Each subplot shows the dispersion of the alloy supercells unfolded back to a $Pnma$ parent structure and the density of states $g(\nu)$ (DoS) as a stacked area plot showing the projection onto Sn (blue), S (purple) and Se atoms (yellow). For the three intermediate compositions, the averaging over structures in the solid-solution model was performed based on a formation temperature T_F of 900 K.

Fig. 4 compares the dispersions and atom-projected DoS curves of the SnS and SnSe endpoints to those of three intermediate compositions with $x_{\text{Se}} = 0.25, 0.5$ and 0.75 . The phonon spectra for the intermediate compositions in Figs. 4c-4e were averaged assuming a 900 K formation temperature (there is only one unique structure for each endpoint, so no averaging is required to generate the spectra in Figs. 4a/4b). A full set of phonon spectra for the nine compositions can be found in Figs. S2-S10.

The spectra of the endpoints each comprise two bands of modes primarily associated with motion of the Sn and chalcogen atoms. At intermediate compositions, the structure of the low-frequency Sn peak is largely unchanged, while the higher-frequency chalcogen feature splits into a mid-frequency Se and high-frequency S component. To a large extent, the Sn sublattice in the mixed phases retains the parent *Pnma* structure, and this is reflected in the low-frequency part of the unfolded dispersions retaining significant detail. On the other hand, substituting the chalcogen atoms spreads out the mid- and high-frequency parts of the dispersion, leading to almost continuous bands in the 50/50 composition with $x_{\text{Se}} = 0.5$.

The broadening of the frequency spectrum at intermediate compositions may have significant implications for the thermal transport, as it could both decrease the mode group velocities and increase the density of energy-conserving phonon scattering events and thereby suppress the mode lifetimes. These points will be returned to in the following subsection.

It can also be seen from the unfolded dispersions and DoS curves that some of the structures in the mixed compositions display imaginary modes. As noted in the previous section, the force constants were calculated to a limited real-space range, and the unfolded dispersions and DoS curves are derived by interpolating the zone-centre (Γ -point) modes of the alloy supercells. None of the structures in the solid-solution model show imaginary modes at the zone centre, which implies that these imaginary modes may indeed be interpolation artefacts. However, evaluating the IFCs in an expanded cell would not be practical given the number of structures in the solid-solution model.

Finally, we also examined the spread in the averaged phonon DoS curves by overlaying the weighted standard deviations (Figs. S11-S19). As suggested by the dispersions of the intermediate compositions in Fig. 4, the calculations predict the spread in the DoS, in particular the chalcogen bands, to increase substantially towards the 50/50 composition. We also generated a series of DoS meshes using the larger $36 \times 24 \times 36$ sampling mesh used to evaluate the vibrational free energies and the tetrahedron method for Brillouin zone integration, which yielded similar overall shapes and predicted spreads (Figs. S20-S28).

c. Implications for thermal transport

Within the single-mode relaxation time approximation (RTA) solution to the Boltzmann transport equation, the macroscopic lattice thermal conductivity tensor κ_{latt} can be calculated as a sum of macroscopic contributions κ_{λ} from individual phonon modes λ according to[37]:

$$\kappa_{\text{latt}} = \frac{1}{NV} \sum_{\lambda} \kappa_{\lambda} = \frac{1}{NV} \sum_{\lambda} C_{\lambda} \mathbf{v}_{\lambda} \otimes \mathbf{v}_{\lambda} \tau_{\lambda} \quad (10)$$

where C_{λ} are the modal heat capacities, \mathbf{v}_{λ} are the group velocities, τ_{λ} are the mode lifetimes, and the macroscopic κ_{latt} is normalised for the unit cell volume V and the number of wavevectors N in the mesh used

to integrate over the Brillouin zone. The product $v_\lambda \tau_\lambda$ is the phonon mean-free path Λ_λ , which appears in a frequently-used variant of Eq. 10. C_λ and v_λ are calculated within the harmonic approximation as:

$$C_\lambda = k_B \left(\frac{\hbar \omega_\lambda}{k_B T} \right)^2 \frac{\exp[-\hbar \omega_\lambda / k_B T]}{(\exp[-\hbar \omega_\lambda / k_B T] - 1)^2} \quad (11)$$

$$v_\lambda = \frac{\partial \omega_\lambda}{\partial \mathbf{q}} = \frac{1}{2\omega_\lambda} \langle \mathbf{W}_\lambda \left| \frac{\partial D(\mathbf{q})}{\partial \mathbf{q}} \right| \mathbf{W}_\lambda \rangle \quad (12)$$

where ω_λ are the mode frequencies, equivalent to the $\omega_{\mathbf{q}v}$ that appear in Eqs. 8 and 9, \mathbf{W}_λ are the corresponding mode eigenvectors, and $D(\mathbf{q})$ is the dynamical matrix for the phonon wavevector \mathbf{q} . τ_λ are the phonon lifetimes and are given by the inverse of the phonon linewidths Γ_λ :

$$\tau_\lambda = \frac{1}{2\Gamma_\lambda} \quad (13)$$

Γ_λ are calculated as the imaginary part of the phonon self-energy, which can be computed perturbatively to third order from:

$$\Gamma_\lambda = \frac{18\pi}{\hbar^2} \sum_{\lambda' \lambda''} |\Phi_{-\lambda \lambda' \lambda''}|^2 \times \{ (n_{\lambda'} + n_{\lambda''} + 1) \delta(\omega_\lambda - \omega_{\lambda'} - \omega_{\lambda''}) + (n_{\lambda'} - n_{\lambda''}) [\delta(\omega_\lambda + \omega_{\lambda'} - \omega_{\lambda''}) - \delta(\omega_\lambda - \omega_{\lambda'} + \omega_{\lambda''})] \} \quad (14)$$

n_λ are the phonon occupation numbers from the Bose-Einstein distribution:

$$n_\lambda = \frac{1}{\exp[-\hbar \omega_\lambda / k_B T] - 1} \quad (15)$$

$\Phi_{\lambda \lambda' \lambda''}$ are the three-phonon interaction strengths calculated from:

$$\begin{aligned}
\Phi_{\lambda\lambda'\lambda''} = & \frac{1}{\sqrt{N}} \frac{1}{3!} \sum_{\kappa\kappa'\kappa''} \sum_{\alpha\beta\gamma} W_{\lambda}(\kappa, \alpha) W_{\lambda'}(\kappa', \beta) W_{\lambda''}(\kappa'', \gamma) \\
& \times \sqrt{\frac{\hbar}{2m_{\kappa}\omega_{\lambda}}} \sqrt{\frac{\hbar}{2m_{\kappa'}\omega_{\lambda'}}} \sqrt{\frac{\hbar}{2m_{\kappa''}\omega_{\lambda''}}} \\
& \times \sum_{l'l''} \Phi_{\alpha\beta\gamma}(0\kappa, l'\kappa', l''\kappa'') \times \exp\{i\mathbf{q}' \cdot [\mathbf{r}(l'\kappa') - \mathbf{r}(0\kappa)]\} \\
& \times \exp\{i\mathbf{q}'' \cdot [\mathbf{r}(l''\kappa'') - \mathbf{r}(0\kappa)]\} \times \exp[i(\mathbf{q} + \mathbf{q}' + \mathbf{q}'') \cdot \mathbf{r}(0\kappa)] \\
& \times \Delta(\mathbf{q} + \mathbf{q}' + \mathbf{q}'')
\end{aligned} \tag{16}$$

The indices κ label atoms with mass m_{κ} and α, β and γ label the Cartesian directions. The third-order IFCs $\Phi_{\alpha\beta\gamma}$ are calculated using the finite-displacement method:

$$\Phi_{\alpha\beta\gamma} = \frac{\partial E}{\partial r_{\alpha} \partial r'_{\beta} \partial r''_{\gamma}} = -\frac{\partial F_{\alpha}}{\partial r'_{\beta} \partial r''_{\gamma}} \approx -\frac{\Delta F_{\alpha}}{\Delta r'_{\beta} \Delta r''_{\gamma}} \tag{17}$$

The indices l label crystallographic unit cells, and the functions δ and Δ enforce conservation of energy and crystal momentum, respectively.

Due to the larger number of pairwise atomic displacements that need to be considered, calculating the third-order IFCs in Eq. 16 to compute the phonon linewidths is typically 1-2 orders of magnitude more computationally expensive than obtaining the second-order force constants for the harmonic phonon calculation, and represents the bulk of the computational workload when modelling κ_{latt} within the RTA.

We have previously modelled the thermal conductivity of *Pnma* SnS and SnSe using the RTA[6,50], based on which we obtained room-temperature (300 K) averaged values of 0.74 and 1.28 W m⁻¹ K⁻¹ respectively. These are in reasonably good agreement with experimental measurements of 1.2 and 0.4-0.7 W m⁻¹ K⁻¹[2,51]. The higher thermal conductivity of the selenide predicted by these calculations is possibly unexpected given the general decrease in κ_{latt} with the formula mass[37], but given the difficulty of preparing high-quality bulk single crystals for measurements it is not clear whether this is a real phenomenon or an issue with the calculations[52,53].

Fig. 5 plots for the two structures the averaged modal contributions to the thermal conductivity $\bar{\kappa}_{\lambda} = \frac{1}{3} \text{Tr}(\kappa_{\lambda})$, the modal heat capacities C_{λ} , the group velocity norms $|\mathbf{v}_{\lambda}|$ and the phonon lifetimes τ_{λ} . In both systems, the $\bar{\kappa}_{\lambda}$ span roughly five orders of magnitude. The heat capacities C_{λ} are a shallow function of frequency and vary by $\sim 10^{-5}$ eV K⁻¹ over the 10 THz range of the SnS phonon spectrum. The \mathbf{v}_{λ} in both systems vary over two orders of magnitude from approx. 10² - 10⁴ ms⁻¹ and are generally higher in the sulphide than the selenide, reflecting the stronger chemical bonding. The mode lifetimes vary by around two orders of magnitude from 0.1 - 10 ps in SnS and 0.5 - 50 ps in SnSe. In both compounds, there is a marked difference in the spectrum of τ_{λ} for the lower- and higher-frequency modes in the phonon spectrum, with the latter being generally shorter lived.

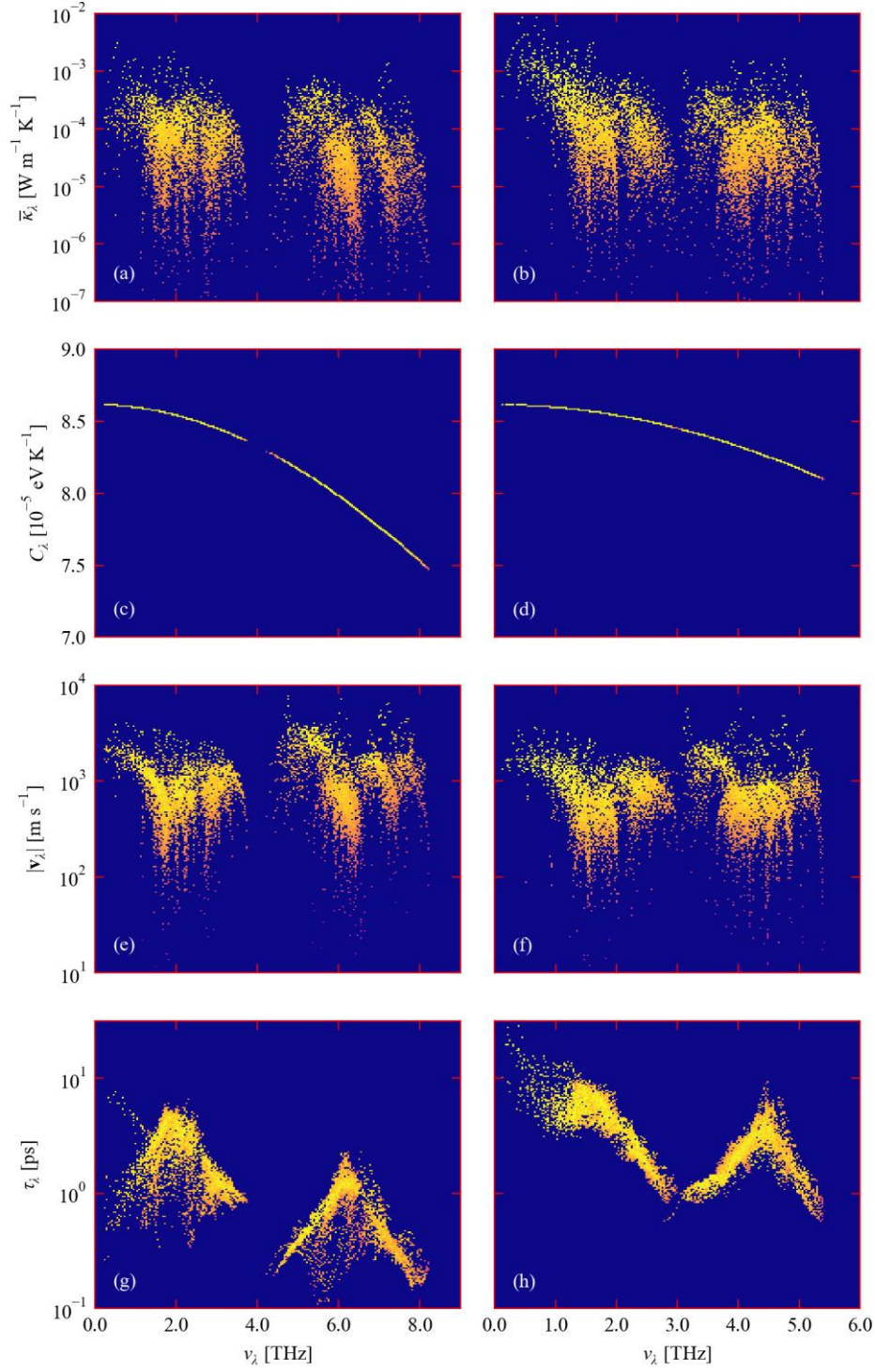


Figure 5 Frequency dependence of the four modal terms in Eq. 10 calculated for SnS (left column) and SnSe (right column): (a)/(b) - averaged thermal conductivities $\bar{\kappa}_\lambda = \frac{1}{3}\text{Tr}(\boldsymbol{\kappa}_\lambda)$; (c)/(d) - heat capacities C_λ ; (e)/(f) - group velocity norms $|v_\lambda|$; (g)/(h) - lifetimes τ_λ . The heat maps are colour coded by $\bar{\kappa}_\lambda$ from red (small $\bar{\kappa}_\lambda$) to yellow (large $\bar{\kappa}_\lambda$). Note that the y axes in subplots (c) and (d) are on a linear scale while the other subplots use a logarithmic scale. The data for SnS and SnSe was generated from the calculations in Refs. [50] and [6] respectively.

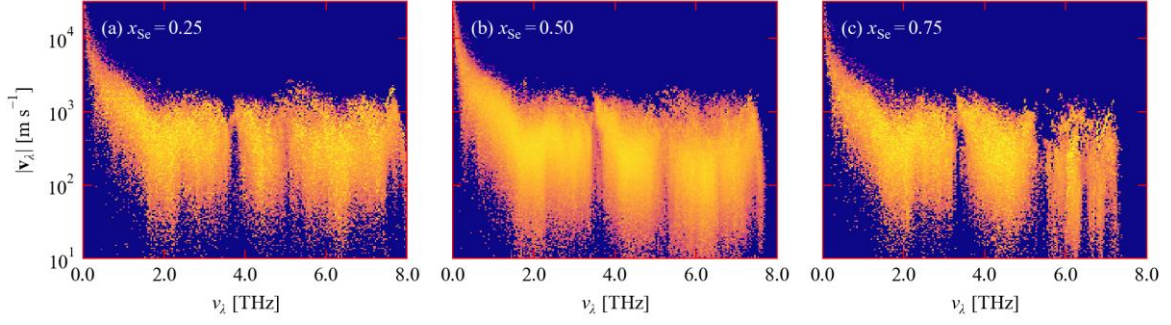


Figure 6 Frequency spectra of the group velocities in $\text{Sn}(\text{S}_{1-x}\text{Se}_x)$ solid solutions with composition $x_{\text{Se}} = 0.25$ (a), 0.5 (b) and 0.75 (c). The colour scale indicates the density of modes and runs from red (low density) to yellow (high density). The averaging over structures in the solid-solution model was performed based on a formation temperature T_{F} of 900 K.

Due to the tensor product $\mathbf{v}_\lambda \otimes \mathbf{v}_\lambda$ in Eq. 10 the $\bar{\kappa}_\lambda$ are proportional to \mathbf{v}_λ^2 and the spectrum of group velocities largely determines the overall spectrum of $\bar{\kappa}_\lambda$. $\bar{\kappa}_\lambda$ are directly proportional to the lifetimes, and the variation in τ_λ with frequency thus imposes additional structure. Comparing SnS and SnSe, it can be seen that the balance of smaller \mathbf{v}_λ but longer τ_λ in the selenide results in similar predicted overall thermal conductivities. The larger averaged thermal conductivity of the SnSe endpoint seems in particular to arise from a group of low-frequency modes ($\nu_\lambda < 1.5$ THz) with group velocities comparable to SnS but with significantly longer lifetimes.

\mathbf{v}_λ are calculated within the harmonic approximation, making it straightforward to compute an averaged frequency spectrum for three of the mixed compositions in the $Pnma$ solid-solution model (Fig. 6). Due to the large number of structures, the \mathbf{v}_λ of each were generated on a small sampling mesh with $5 \times 3 \times 5$ subdivisions. Tests on the SnS and SnSe endpoints using an equivalent $9 \times 3 \times 10$ sampling mesh yielded 300 K thermal conductivities to within 5 % of the values obtained with the larger $16 \times 16 \times 16$ meshes used in the previous studies[6,50]. Comparing the spectra of the mixed compositions with $x_{\text{Se}} = 0.25, 0.5$ and 0.75 to the pure SnS and SnSe endpoints in Fig. 5 clearly shows that the alloying results in a much broader distribution of \mathbf{v}_λ . The high group velocities of the low-frequency modes are maintained, and the bulk of the modes fall into the same 10^2 - 10^3 m s^{-1} range as the endpoints, but there is a general shift to lower \mathbf{v}_λ among the mid- and high-frequency modes, which becomes more prominent for larger x_{Se} . Comparison of the \mathbf{v}_λ of the full range of compositions (Figs. S29-S37) further highlights the larger spread of group velocities at intermediate compositions, mirroring the broadening of the phonon spectra in Fig. 4.

We note that we are comparing data for the mixed compositions to previous calculations performed without a dispersion correction and using larger supercell expansions to calculate the force constants. In general, the main impact of the exchange-correlation functional on the lattice dynamics is through differences in the predicted equilibrium volume[54]. The optimised volumes of SnS and SnSe obtained in Refs. [6] and [50] are similar to those of the two endpoints in our solid-solution model ($46.9/45.8$ and $51.8/50.7$ \AA^3 per F.U. respectively), so we do not expect this to be big issue. However, the larger supercell expansion used in the endpoint calculations will in principle make the calculated \mathbf{v}_λ more accurate by improving the accuracy of the interpolated dispersion and hence the derivatives $\mathbf{v}_\lambda = \partial\omega_\lambda/\partial\mathbf{q}$ (c. f. Eq. 12). This may in particular explain why some of the lower-frequency modes in the mixed compositions are predicted to reach higher $|\mathbf{v}_\lambda|$ than in either of the endpoints, which is otherwise unexpected.

Due to the significantly higher cost of calculating the third-order IFCs, explicitly computing the lifetimes of even a subset of the solid solution models is impractical. However, it is possible to obtain some qualitative insight into how the alloying may affect the heat transport from the (harmonic) phonon DoS. As noted above, the phonon lifetimes in Eq. 10 are calculated from the phonon linewidths Γ_λ (Eq. 13), which are in turn computed as a sum of contributions from three-phonon scattering processes with pairs of modes λ' and λ'' (Eq. 14) that depend on the three-phonon interaction strength $|\Phi_{\lambda\lambda'\lambda''}|^2$, the mode occupation numbers and the difference in the phonon frequencies. An approximate linewidth $\tilde{\Gamma}_\lambda$ can thus be written as the product of an averaged phonon interaction strength P_λ and a joint density of states $N_2(\mathbf{q}, \omega)$ (JDoS) counting the number of energy-conserving scattering channels as a function of frequency:[37]

$$\tilde{\Gamma}_\lambda = \frac{18\pi}{\hbar^2} P_\lambda N_2(\mathbf{q}_\lambda, \omega_\lambda) \quad (18)$$

The interaction strength P_λ is defined as:

$$P_\lambda = \frac{1}{(3n_a)^2} \sum_{\lambda'\lambda''} |\Phi_{\lambda\lambda'\lambda''}|^2 \quad (19)$$

where n_a is the number of atoms in the primitive cell and $3n_a$ is the number of bands at each phonon wavevector. The JDoS $N_2(\mathbf{q}, \omega)$ is a sum of two functions corresponding to collision (Type 1 - two phonons in, one out) and decay processes (Type 2 - one phonon in, two out):

$$N_2(\mathbf{q}_\lambda, \omega_\lambda) = N_2^{(1)}(\mathbf{q}_\lambda, \omega_\lambda) + N_2^{(2)}(\mathbf{q}_\lambda, \omega_\lambda) \quad (20)$$

$N_2^{(1)}(\mathbf{q}_\lambda, \omega_\lambda)$ and $N_2^{(2)}(\mathbf{q}_\lambda, \omega_\lambda)$ are defined as follows:

$$N_2^{(1)}(\mathbf{q}_\lambda, \omega_\lambda) = \frac{1}{N} \sum_{\lambda'\lambda''} \Delta(-\mathbf{q} + \mathbf{q}' + \mathbf{q}'') (n_{\lambda'} - n_{\lambda''}) \times [\delta(\omega + \omega_{\lambda'} - \omega_{\lambda''}) - \delta(\omega - \omega_{\lambda'} + \omega_{\lambda''})] \quad (21)$$

$$N_2^{(2)}(\mathbf{q}_\lambda, \omega_\lambda) = \frac{1}{N} \sum_{\lambda'\lambda''} \Delta(-\mathbf{q} + \mathbf{q}' + \mathbf{q}'') (n_{\lambda'} + n_{\lambda''} + 1) \times \delta(\omega - \omega_{\lambda'} - \omega_{\lambda''}) \quad (22)$$

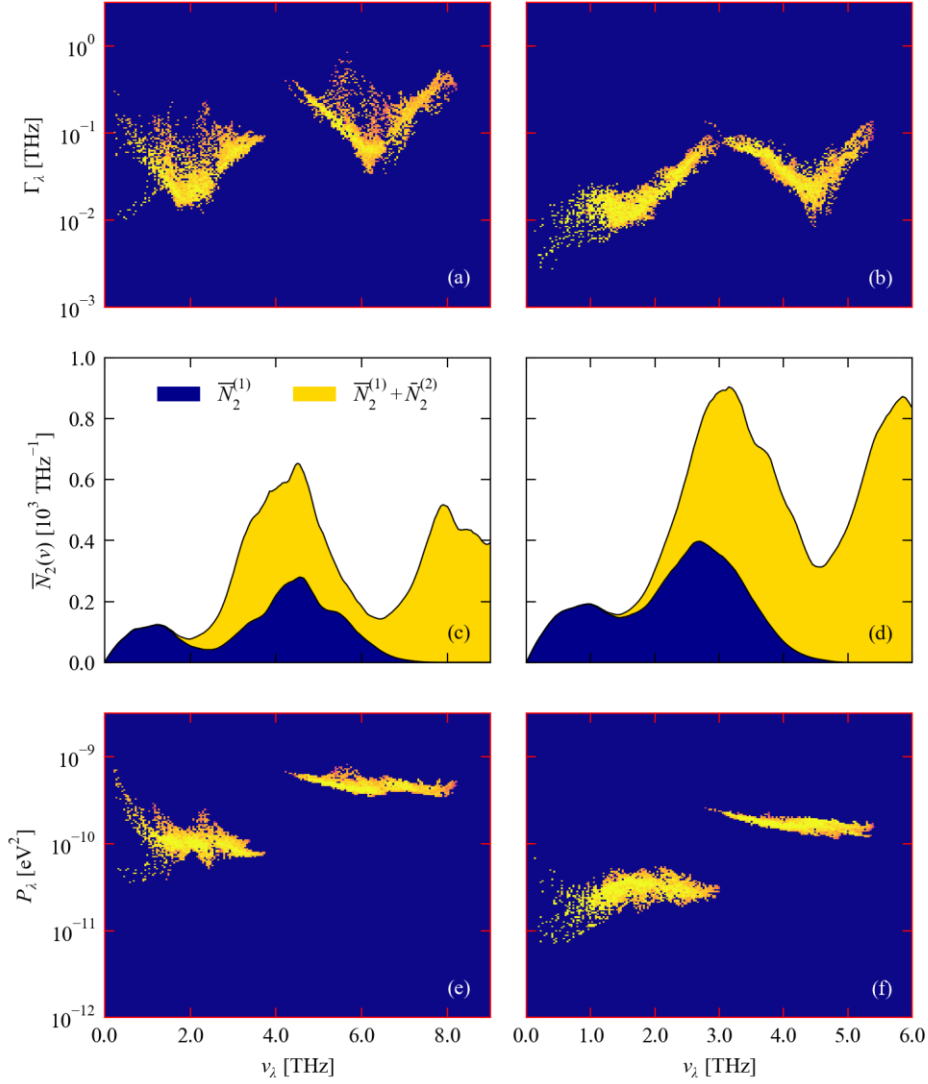


Figure 7 Analysis of the phonon lifetimes in SnS (left column) and SnSe (right column) using Eqs. 18-23: (a)/(b) - mode linewidths Γ_λ as a function of frequency; (c)/(d) - two-phonon density of states $\bar{N}_2(\nu)$ shown separately for collision (Type 1 - $\bar{N}_2^{(1)}$) and decay (Type 2 - $\bar{N}_2^{(2)}$) events; (e)/(f) - averaged three-phonon interaction strengths P_λ . As in Fig. 5 the heat maps are colour coded by $\bar{\kappa}_\lambda$ from red (small $\bar{\kappa}_\lambda$) to yellow (large $\bar{\kappa}_\lambda$). Note that the y-axes in subplots (c) and (d) are on a linear scale while the other subplots use a logarithmic scale. As in Fig. 5 the data for SnS and SnSe was generated from the calculations in Refs. [50] and [6] respectively.

n_λ are the phonon occupation numbers at the calculation temperature (Eq. 15) and the functions δ and Δ enforce conservation of energy and crystal momentum, respectively (c.f. Eqs. 14/16). Finally, we further define a function $\bar{N}_2(\omega_\lambda)$ and component parts $\bar{N}_2^{(1)}(\omega_\lambda)$ and $\bar{N}_2^{(2)}(\omega_\lambda)$ averaged over wavevectors \mathbf{q} as follows:

$$\bar{N}_2(\omega_\lambda) = \bar{N}_2^{(1)}(\omega_\lambda) + \bar{N}_2^{(2)}(\omega_\lambda) = \frac{1}{N} \sum_{\mathbf{q}} N_2^{(1)}(\mathbf{q}_\lambda, \omega_\lambda) + \frac{1}{N} \sum_{\mathbf{q}} N_2^{(2)}(\mathbf{q}_\lambda, \omega_\lambda) \quad (23)$$

The JDoS functions are calculable from the harmonic phonon frequencies and, if the P_λ can be assumed to be similar in the intermediate phases and endpoints, could provide an indication of the expected composition dependence of the phonon lifetimes. Figure 7 compares the spectrum of phonon linewidths of the SnS and SnSe endpoints against the JDoS functions and the P_λ . The distribution of Γ_λ reflects the trends in the lifetimes shown in Fig. 5: in both spectra, the higher-frequency bands of modes show broader linewidths (shorter lifetimes) than the lower-frequency modes, and the sulphide shows broader linewidths than the selenide. Comparison of the linewidth spectra against $\bar{N}_2(\omega_\lambda)$ shows that variation in the density of energy-conserving scattering pathways with frequency is largely responsible for the overall structure, with peaks in $\bar{N}_2(\omega_\lambda)$ overlapping with increases in Γ_λ . Collision (Type 1) and decay (Type 2) events are the dominant scattering processes at low and high frequencies, respectively, while both processes are active at intermediate frequencies. On the other hand, differences in the magnitude of the phonon interaction strengths are clearly responsible for the marked difference in the linewidths of the low- and high-frequency bands of modes, and the lower P_λ in the selenide counteract the increase in the JDoS, resulting in narrower linewidths (longer lifetimes) than in the sulphide.

Comparing the $\bar{N}_2(\omega_\lambda)$ of the SnS and SnSe endpoints to averaged JDoS functions calculated for the intermediate compositions (Fig. 8) shows the effect of spreading the phonon DoS over a larger range of frequencies (c.f. Fig. 4). Whereas in the SnS and SnSe endpoints the two JDoS functions $\bar{N}_2^{(1)}$ and $\bar{N}_2^{(2)}$ show distinct peaks due to the well-defined bands of modes in the respective phonon spectra, the JDoS functions of the mixed compositions are much broader, implying stronger scattering across a broad spectrum of mid- and high-frequency modes. However, the calculations predict the JDoS of all three mixed compositions to be on a similar scale to the endpoints, which suggests that the broader range of phonon frequencies in the mixed compositions does not necessarily lead to as large an enhancement in the number of scattering channels as might be expected. This is, however, consistent with the relatively small absolute variation in κ_{latt} observed among different alloy compositions in experiments[12,14].

The analysis in Fig. 5 suggests that the majority of the heat transport is through low-frequency modes with large group velocities and long lifetimes. The calculated JDoS functions for the mixed phases suggest an overall increase in the density of both collision and decay pathways for modes up to ~ 2 THz compared to the endpoints. For SnS this can be ascribed to chalcogen substitution introducing low-lying optic modes to participate in collision processes, whereas for SnSe the dominant effect is most likely the broadening of the mid-frequency Se phonon bands creating additional scattering channels. In both cases, the small increase in the number of scattering channels would be expected to result in some suppression of heat transport in the alloy, consistent with experimental findings. However, based on the analysis in Fig. 7 we would expect differences in the interaction strengths P_λ with composition to have a prominent effect on the heat transport and, as it is not feasible to investigate this further, we therefore treat this finding with caution.

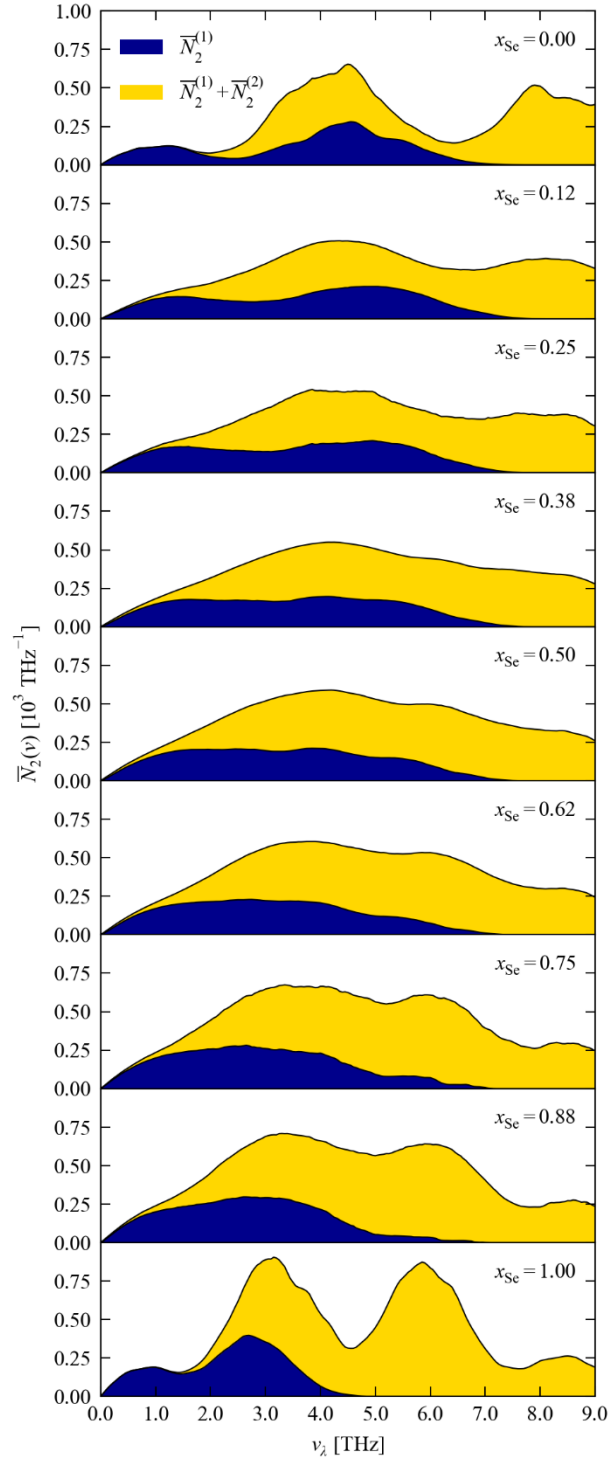


Figure 8 Averaged two-phonon joint density of states (JDoS) $\bar{N}_2(\nu)$ for $\text{Sn}(\text{S}_{1-x}\text{Se}_x)$ solid solutions with composition x_{Se} ranging from 0 (SnS) to 1 (SnSe). Each plot shows the JDoS for collision (Type 1 - $\bar{N}_2^{(1)}$) and decay (Type 2 - $\bar{N}_2^{(2)}$) events separately. The data in Fig. 7 for the SnS and SnSe endpoints is included for comparison and was generated using the previous calculations in Refs. [6] and [50]. For the intermediate compositions, the averaging over structures in the solid-solution model was performed based on a formation temperature T_F of 900 K.

Conclusions

This work has presented a detailed investigation of the lattice dynamics in *Pnma* $\text{Sn}(\text{S}_{1-x}\text{Se}_x)$ solid solutions and the impact of the dynamics on the energetics and thermal transport.

Our calculations show that the phonon free energy makes a significant contribution to the thermodynamic partition function, in this case leading to a reduction in the mixing energy and a marked difference in the distribution of occurrence probabilities among individual configurations in the alloy model. Here the qualitative stability of the mixed phases remains unchanged, and the similar electrical properties of the individual structures in the mixed compositions results in negligible changes to the averaged bandgaps. However, given the size of the effects predicted by the calculations, it is very likely that the lattice dynamics could have a significant qualitative impact in other systems, particularly those with energetically-similar competing phases, as has been observed in other work[43,47]. In the case of the $\text{Sn}_n(\text{S}_{1-x}\text{Se}_x)_m$, it is possible that differences in lattice dynamics may bring the metastable rocksalt phase closer to the $\text{Sn}(\text{S}_{1-x}\text{Se}_x)$ convex hull at intermediate compositions and/or stabilise the sesquisulphide $\text{Sn}_2(\text{S}_{1-x}\text{Se}_x)_3$ relative to the competing mono- and di-chalcogenide phases, but we defer exploration of this to future work.

Comparing the unfolded phonon dispersions and density of states over the range of compositions shows a clear pattern whereby the well-defined bands of high- and mid-frequency S/Se modes in the SnS and SnSe endpoints, respectively, are spread over a wider range of frequencies while the band structure of the low-frequency Sn modes is largely retained. This results in some lowering of the group velocities and produces additional energy-conserving scattering channels in the joint density of states, both of which could in principle reduce the thermal conductivity in the mixed phases. However, comparison of the endpoints suggests that differences in the three-phonon interaction strengths make a significant contribution to the difference in heat transport between them, and it is not practical at present to investigate how these are affected by alloying.

This leads us to close by noting several challenges to this type of study that should be addressed in future work. The practical restriction of calculating the harmonic force constants in the 32-atom alloy supercells is likely to restrict the accuracy of calculated phonon spectra and derived properties such as the free energies and group velocities. In general, this issue may be further exacerbated by potentially needing to reduce the plane-wave cutoff and k -point sampling in alloy calculations to minimise the computational cost. Secondly, more accurate free energies could be obtained by taking into account the volume expansion at finite temperature using the quasi-harmonic approximation, but to perform QHA calculations for the full set of structures in a complex alloy such as *Pnma* SnS is not currently practical using first-principles methods. Finally, as noted above, our analysis of the thermal conductivity of the SnS and SnSe endpoints indicates that differences in the phonon interaction strengths are likely to be a significant contributor to the differences between the compounds, but to quantify this requires computing the third-order force constants which is again not practical even for a small subset of the structures.

Several routes to address these challenges can be envisaged. The cost of the first-principles calculations could be reduced by using alternatives to plane-wave DFT, for example periodic codes using efficient local-orbital or LCAO approaches[55–57]. Alternatively and/or in addition to this, a sampling approach could be employed to obtain the second- and/or third-order force constants using a smaller set of explicit calculations. The relatively predictable set of chemical environments in an alloy should also make them amenable to modelling with force fields, which could be parameterised against a smaller subset of first-principles calculations in the spirit of the aforementioned sampling approach.

Nonetheless, this study has demonstrated that studying the lattice dynamics of relatively complex solid solutions is within the reach of contemporary first-principles modelling, and has highlighted some of the ways

in which changes in the dynamics with composition can influence both the stability of mixed phases and important physical properties for applications such as thermoelectric power.

Acknowledgements

JMS gratefully acknowledges the support of a Presidential Fellowship from the University of Manchester and assistance from A. Togo (Kyoto) with using the band-unfolding routines in Phonopy. The majority of the DFT calculations in this work were performed using the UK Archer HPC facility, *via* membership of the UK Materials Chemistry Consortium, which is funded by the UK Engineering and Physical Sciences Research Council (EPSRC; grant nos. EP/L000202 and EP/R029431). The post processing with Phonopy was carried out using the University of Manchester Computational Shared Facility (CSF) HPC cluster, which is supported and maintained by UoM Research IT.

References

- [1] Tan G, Zhao L-D and Kanatzidis M G 2016 Rationally Designing High-Performance Bulk Thermoelectric Materials *Chem. Rev.* **116** 12123–49
- [2] Tan Q, Zhao L-D, Li J-F, Wu C-F, Wei T-R, Xing Z-B and Kanatzidis M G 2014 Thermoelectrics with earth abundant elements: low thermal conductivity and high thermopower in doped SnS *J. Mater. Chem. A* **2** 17302–6
- [3] Nolas G S, Sharp J and Goldsmid H J 2001 The Phonon-Glass Electron-Crystal Approach to Thermoelectric Materials Research *Thermoelectrics* (Berlin/Heidelberg: Springer-Verlag) pp 177–207
- [4] Delaire O, Ma J, Marty K, May A F, McGuire M A, Du M-H, Singh D J, Podlesnyak A, Ehlers G, Lumsden M D and C S B 2011 Giant anharmonic phonon scattering in PbTe. *Nat. Mater.* **10** 614–9
- [5] Li C W, Hong J, May A F, Bansal D, Chi S, Hong T, Ehlers G and Delaire O 2015 Orbitally driven giant phonon anharmonicity in SnSe *Nat. Phys.* **11** 1063–9
- [6] Skelton J M, Burton L A, Parker S C, Walsh A, Kim C-E, Soon A, Buckeridge J, Sokol A A, Catlow C R A, Togo A and Tanaka I 2016 Anharmonicity in the High-Temperature *Cmcm* Phase of SnSe: Soft Modes and Three-Phonon Interactions *Phys. Rev. Lett.* **117** 075502
- [7] Koumoto K, Wang Y, Zhang R, Kosuga A and Funahashi R 2010 Oxide Thermoelectric Materials: A Nanostructuring Approach *Annu. Rev. Mater. Res.* **40** 363–94
- [8] Koumoto K, Funahashi R, Guilmeau E, Miyazaki Y, Weidenkaff A, Wang Y and Wan C 2013 Thermoelectric Ceramics for Energy Harvesting ed X-D Zhou *J. Am. Ceram. Soc.* **96** 1–23
- [9] Mehdizadeh Dehkordi A, Zebarjadi M, He J and Tritt T M 2015 Thermoelectric power factor: Enhancement mechanisms and strategies for higher performance thermoelectric materials *Mater. Sci. Eng. R Reports* **97** 1–22
- [10] Ou C, Hou J, Wei T R, Jiang B, Jiao S, Li J F and Zhu H 2015 High thermoelectric performance of all-oxide heterostructures with carrier double-barrier filtering effect *NPG Asia Mater.* **7**
- [11] Shibuya T, Skelton J M, Jackson A J, Yasuoka K, Togo A, Tanaka I and Walsh A 2016 Suppression of lattice thermal conductivity by mass-conserving cation mutation in multi-component semiconductors *APL Mater.* **4** 104809
- [12] Han Y-M, Zhao J, Zhou M, Jiang X-X, Leng H-Q and Li L-F 2015 Thermoelectric performance of SnS and

SnS–SnSe solid solution *J. Mater. Chem. A* **3** 4555–9

- [13] Asfandiyar, Wei T-R, Li Z, Sun F-H, Pan Y, Wu C-F, Farooq M U, Tang H, Li F, Li B and Li J-F 2017 Thermoelectric SnS and SnS-SnSe solid solutions prepared by mechanical alloying and spark plasma sintering: Anisotropic thermoelectric properties *Sci. Rep.* **7** 43262
- [14] Lin C-C, Lydia R, Yun J H, Lee H S and Rhyee J S 2017 Extremely Low Lattice Thermal Conductivity and Point Defect Scattering of Phonons in Ag-doped $(\text{SnSe})_{1-x}(\text{SnS})_x$ Compounds *Chem. Mater.* **29** 5344–52
- [15] Witting I T, Chasapis T C, Ricci F, Peters M, Heinz N A, Hautier G and Snyder G J 2019 The Thermoelectric Properties of Bismuth Telluride *Adv. Electron. Mater.* **5** 1800904
- [16] Sun J, Su X, Yan Y, Liu W, Tan G and Tang X 2019 Enhancing Thermoelectric Performance of n-Type PbSe through Forming Solid Solution with PbTe and PbS *ACS Appl. Energy Mater.* [acsaem.9b01656](https://doi.org/10.1021/acsaem.9b01656)
- [17] Tian Z, Garg J, Esfarjani K, Shiga T, Shiomi J and Chen G 2012 Phonon conduction in PbSe, PbTe, and $\text{PbTe}_{1-x}\text{Se}_x$ from first-principles calculations *Phys. Rev. B - Condens. Matter Mater. Phys.* **85**
- [18] Butler K T, Frost J M, Skelton J M, Svane K L and Walsh A 2016 Computational materials design of crystalline solids *Chem. Soc. Rev.* **45**
- [19] Skelton J M, Parker S C, Togo A, Tanaka I and Walsh A 2014 Thermal physics of the lead chalcogenides PbS, PbSe, and PbTe from first principles *Phys. Rev. B* **89** 205203
- [20] Aseginolaza U, Bianco R, Monacelli L, Paulatto L, Calandra M, Mauri F, Bergara A and Errea I 2019 Phonon Collapse and Second-Order Phase Transition in Thermoelectric SnSe *Phys. Rev. Lett.* **122**
- [21] Zhu L, Jiang X, Gao G, Fu H and Yao K 2018 First-Principles Study on the Thermoelectric Properties of FeAsS *ACS Omega* **3** 13630–5
- [22] Shiga T, Shiomi J, Ma J, Delaire O, Radzynski T, Lusakowski A, Esfarjani K and Chen G 2012 Microscopic mechanism of low thermal conductivity in lead telluride *Phys. Rev. B - Condens. Matter Mater. Phys.* **85**
- [23] Zhang Y, Ke X, Chen C, Yang J and Kent P R C 2009 Thermodynamic properties of PbTe, PbSe, and PbS: First-principles study *Phys. Rev. B - Condens. Matter Mater. Phys.* **80**
- [24] Gorai P, Toberer E S and Stevanović V 2016 Computational identification of promising thermoelectric materials among known quasi-2D binary compounds *J. Mater. Chem. A* **4** 11110–6
- [25] Li R, Li X, Xi L, Yang J, Singh D J and Zhang W 2019 High-Throughput Screening for Advanced Thermoelectric Materials: Diamond-Like ABX_2 Compounds *ACS Appl. Mater. Interfaces* **11** 24859–66
- [26] Gunn D S D, Skelton J M, Burton L A, Metz S and Parker S C 2019 Thermodynamics, Electronic Structure, and Vibrational Properties of $\text{Sn}_n(\text{S}_{1-x}\text{Se}_x)_m$ Solid Solutions for Energy Applications *Chem. Mater.* **31** 3672–85
- [27] Ektarawong A and Alling B 2018 Stability of $\text{SnSe}_{1-x}\text{S}_x$ solid solutions revealed by first-principles cluster expansion *J. Phys. Condens. Matter* **30** 29LT01
- [28] Grau-Crespo R, Hamad S, Catlow C R A and de Leeuw N H 2007 Symmetry-adapted configurational modelling of fractional site occupancy in solids *J. Phys. Condens. Matter* **19** 256201
- [29] Jain A, Voznyy O and Sargent E H 2017 High-Throughput Screening of Lead-Free Perovskite-like Materials for Optoelectronic Applications *J. Phys. Chem. C* **121** 7183–7
- [30] Emery A A, Saal J E, Kirklin S, Hegde V I and Wolverton C 2016 High-Throughput Computational Screening of Perovskites for Thermochemical Water Splitting Applications *Chem. Mater.* **28** 5621–34
- [31] Wu Y, Lazic P, Hautier G, Persson K and Ceder G 2013 First principles high throughput screening of

oxynitrides for water-splitting photocatalysts *Energy Environ. Sci.* **6** 157–68

- [32] Brunin G, Ricci F, Ha V A, Rignanese G M and Hautier G 2019 Transparent conducting materials discovery using high-throughput computing *npj Comput. Mater.* **5**
- [33] Seko A, Togo A, Hayashi H, Tsuda K, Chaput L and Tanaka I 2015 Prediction of Low-Thermal-Conductivity Compounds with First-Principles Anharmonic Lattice-Dynamics Calculations and Bayesian Optimization *Phys. Rev. Lett.* **115**
- [34] Skelton J M 2017 Transformer
- [35] Togo A and Tanaka I 2015 First principles phonon calculations in materials science *Scr. Mater.* **108** 1–5
- [36] Allen P B, Berlijn T, Casavant D A and Soler J M 2013 Recovering hidden Bloch character: Unfolding electrons, phonons, and slabs *Phys. Rev. B - Condens. Matter Mater. Phys.* **87**
- [37] Togo A, Chaput L and Tanaka I 2015 Distributions of phonon lifetimes in Brillouin zones *Phys. Rev. B* **91** 094306
- [38] Kresse G and Hafner J 1993 Ab initio molecular dynamics for liquid metals *Phys. Rev. B* **47** 558(R)-561(R)
- [39] Monkhorst H J and Pack J D 1976 Special points for Brillouin-zone integrations *Phys. Rev. B* **13** 5188–92
- [40] Blöchl P E 1994 Projector augmented-wave method *Phys. Rev. B* **50** 17953–79
- [41] Kresse G and Joubert D 1999 From ultrasoft pseudopotentials to the projector augmented-wave method *Phys. Rev. B* **59** 1758–75
- [42] Skelton J M, Burton L A, Oba F and Walsh A 2017 Chemical and Lattice Stability of the Tin Sulfides *J. Phys. Chem. C* **121** 6446–54
- [43] Van de Walle A and Ceder G 2002 The effect of lattice vibrations on substitutional alloy thermodynamics *Rev. Mod. Phys.* **74** 11–45
- [44] Pallipurath A R, Skelton J M, Warren M R, Kamali N, McArdle P and Erxleben A 2015 Sulfamerazine: Understanding the influence of slip planes in the polymorphic phase transformation through x-ray crystallographic studies and ab initio lattice dynamics *Mol. Pharm.* **12**
- [45] Kieslich G, Skelton J M, Armstrong J, Wu Y, Wei F, Svane K L, Walsh A and Butler K T 2018 Hydrogen Bonding versus Entropy: Revealing the Underlying Thermodynamics of the Hybrid Organic–Inorganic Perovskite $[\text{CH}_3\text{NH}_3]\text{PbBr}_3$ *Chem. Mater.* **30** 8782–8
- [46] Butler K T, Vervoorts P, Ehrenreich M G, Armstrong J, Skelton J M and Kieslich G 2019 Experimental Evidence for Vibrational Entropy as Driving Parameter of Flexibility in the Metal–Organic Framework ZIF-4(Zn) *Chem. Mater.* **31** 8366–72
- [47] Burton B P and van de Walle A 2006 First-principles phase diagram calculations for the system NaCl-KCl: The role of excess vibrational entropy *Chem. Geol.* **225** 222–9
- [48] Van De Walle A 2013 Methods for first-principles alloy thermodynamics *JOM* **65** 1523–32
- [49] Todorov I T, Allan N L, Lavrentiev M Y, Freeman C L, Mohn C E and Purton J A 2004 Simulation of mineral solid solutions at zero and high pressure using lattice statics, lattice dynamics and Monte Carlo methods *J. Phys. Condens. Matter* **16** S2751–70
- [50] Skelton J M, Burton L A, Jackson A J, Oba F, Parker S C and Walsh A 2017 Lattice dynamics of the tin sulphides SnS_2 , SnS and Sn_2S_3 : Vibrational spectra and thermal transport *Phys. Chem. Chem. Phys.* **19** 12452–65
- [51] Zhao L-D, Lo S-H, Zhang Y, Sun H, Tan G, Uher C, Wolverton C, Dravid V P and Kanatzidis M G 2014

Ultralow thermal conductivity and high thermoelectric figure of merit in SnSe crystals *Nature* **508** 373–7

- [52] Wei P-C, Bhattacharya S, He J, Neeleshwar S, Podila R, Chen Y Y and Rao A M 2016 Brief Communications Arising The intrinsic thermal conductivity of SnSe *Nature* **377** 2014–6
- [53] Zhao L D, Lo S H, Zhang Y, Sun H, Tan G, Uher C, Wolverton C, Dravid V P and Kanatzidis M G 2016 Zhao et al. reply *Nature* **539** E2–3
- [54] Skelton J M, Tiana D, Parker S C, Togo A, Tanaka I and Walsh A 2015 Influence of the exchange-correlation functional on the quasi-harmonic lattice dynamics of II-VI semiconductors *J. Chem. Phys.* **143**
- [55] Blum V, Gehrke R, Hanke F, Havu P, Havu V, Ren X, Reuter K and Scheffler M 2009 Ab initio molecular simulations with numeric atom-centered orbitals *Comput. Phys. Commun.* **180** 2175–96
- [56] Dovesi R, Erba A, Orlando R, Zicovich-Wilson C M, Civalleri B, Maschio L, Rérat M, Casassa S, Baima J, Salustro S and Kirtman B 2018 Quantum-mechanical condensed matter simulations with CRYSTAL *Wiley Interdiscip. Rev. Comput. Mol. Sci.* **8** e1360
- [57] Larsen A H, Vanin M, Mortensen J J, Thygesen K S and Jacobsen K W 2009 Localized atomic basis set in the projector augmented wave method *Phys. Rev. B - Condens. Matter Mater. Phys.* **80**

Lattice dynamics of *Pnma* Sn(S_{1-x}Se_x) solid solutions: energetics, phonon spectra and thermal transport

Electronic supporting information

Jonathan M. Skelton^{1*}

¹ *Department of Chemistry, University of Manchester, Oxford Road, Manchester M13 9PL, UK*

* Corresponding author - e-mail jonathan.skelton@manchester.ac.uk

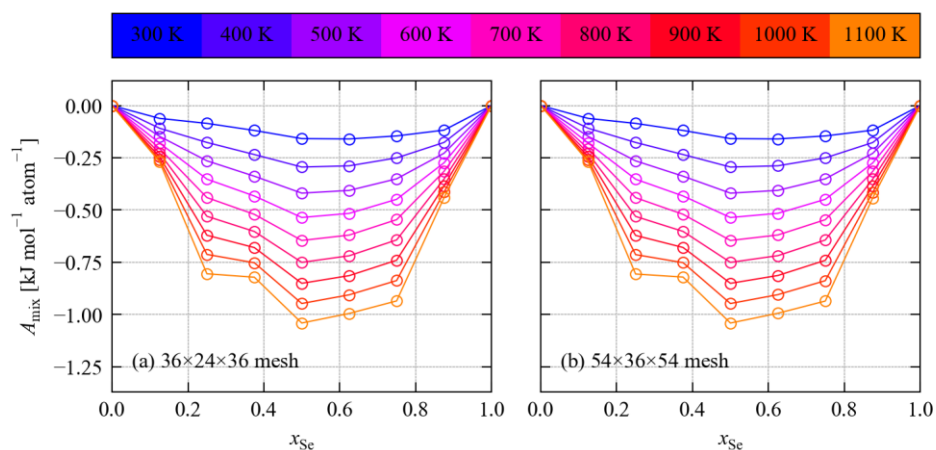


Figure S1 Calculated mixing free energies A_{mix} of *Pnma* $\text{Sn}(\text{S}_{1-x}\text{Se}_x)$ solid solutions as a function of Se fraction x_{Se} , obtained using the Helmholtz free energies A_n with the vibrational contributions evaluated using Brillouin zone sampling meshes with $36 \times 24 \times 26$ (a) and $54 \times 36 \times 54$ subdivisions (b). The data in (a) is the same as that in Fig. 1b in the text. Both plots show $A_{\text{mix}}(x_{\text{Se}})$ for a range of alloy formation temperatures T_{F} from 300 - 1100 K, which are denoted by line colours from blue (low T_{F}) to orange (high T_{F}).

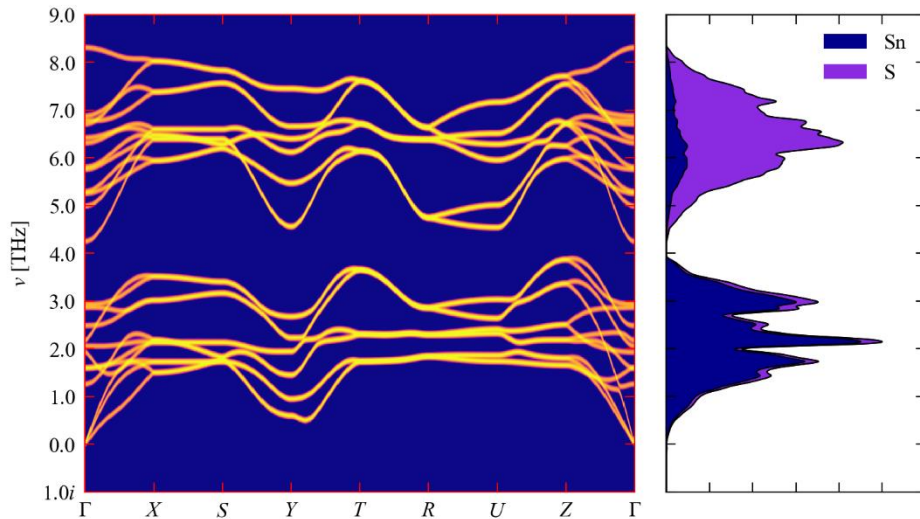


Figure S2 Simulated phonon spectra of *Pnma* SnS. The left-hand panel shows the phonon dispersion and the right-hand panel shows the density of states $g(\nu)$ (DoS) as a stacked area plot with the projections onto Sn (blue) and S atoms (purple).

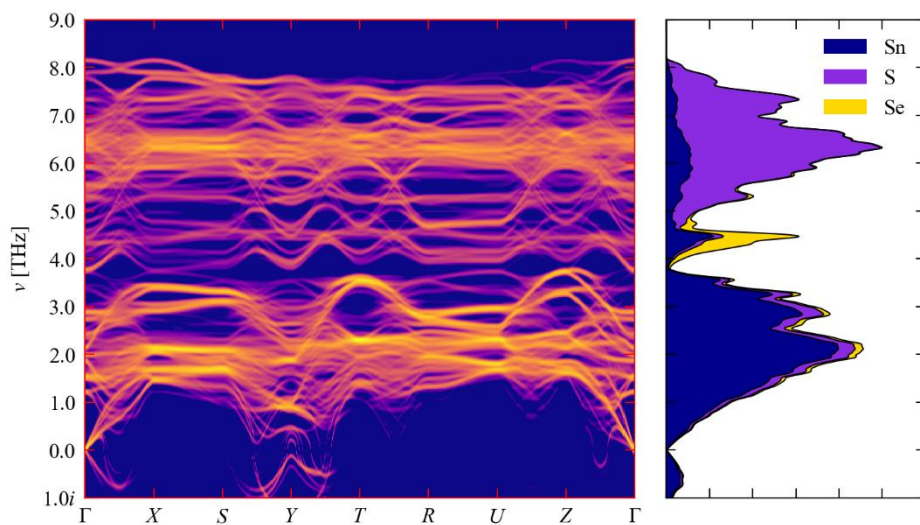


Figure S3 Simulated phonon spectra of a *Pnma* $\text{SnS}_{0.875}\text{Se}_{0.125}$ solid solution. The left-hand panel shows the phonon dispersion unfolded back to a *Pnma* parent structure. The right-hand panel shows the density of states $g(\nu)$ (DoS) as a stacked area plot with the projections onto Sn (blue), S (purple) and Se atoms (yellow). The averaging over structures in the solid-solution model was performed based on a formation temperature T_F of 900 K.

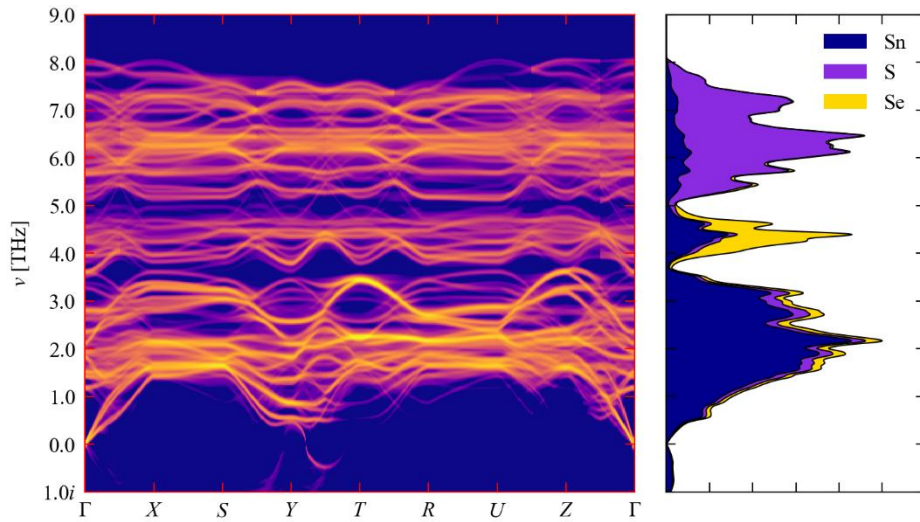


Figure S4 Simulated phonon spectra of a *Pnma* $\text{SnS}_{0.75}\text{Se}_{0.25}$ solid solution. The left-hand panel shows the phonon dispersion unfolded back to a *Pnma* parent structure. The right-hand panel shows the density of states $g(\nu)$ (DoS) as a stacked area plot with the projections onto Sn (blue), S (purple) and Se atoms (yellow). The averaging over structures in the solid-solution model was performed based on a formation temperature T_F of 900 K.

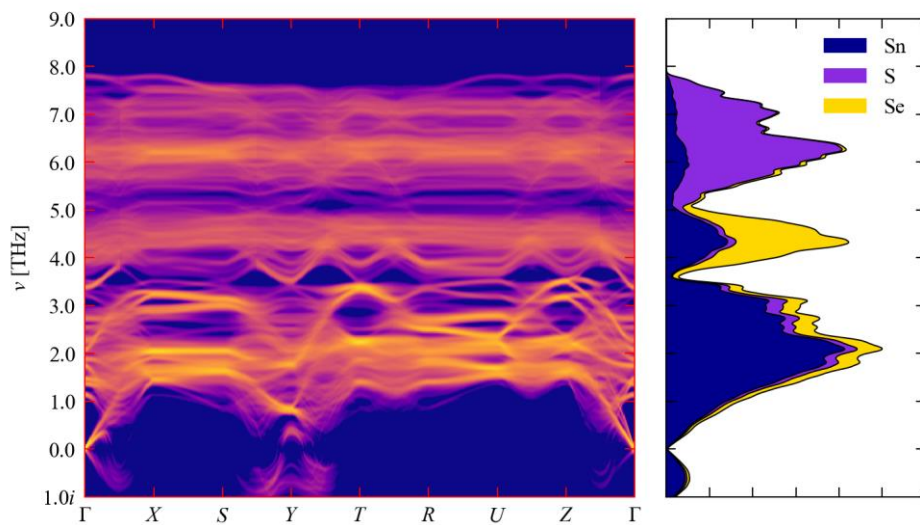


Figure S5 Simulated phonon spectra of a *Pnma* $\text{SnS}_{0.625}\text{Se}_{0.375}$ solid solution. The left-hand panel shows the phonon dispersion unfolded back to a *Pnma* parent structure. The right-hand panel shows the density of states $g(\nu)$ (DoS) as a stacked area plot with the projections onto Sn (blue), S (purple) and Se atoms (yellow). The averaging over structures in the solid-solution model was performed based on a formation temperature T_F of 900 K.

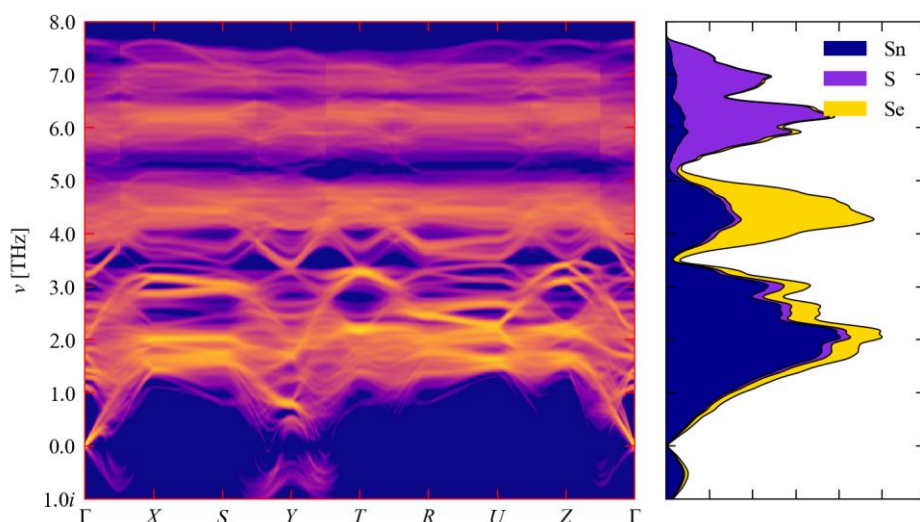


Figure S6 Simulated phonon spectra of a *Pnma* $\text{SnS}_{0.5}\text{Se}_{0.5}$ solid solution. The left-hand panel shows the phonon dispersion unfolded back to a *Pnma* parent structure. The right-hand panel shows the density of states $g(\nu)$ (DoS) as a stacked area plot with the projections onto Sn (blue), S (purple) and Se atoms (yellow). The averaging over structures in the solid-solution model was performed based on a formation temperature T_F of 900 K.

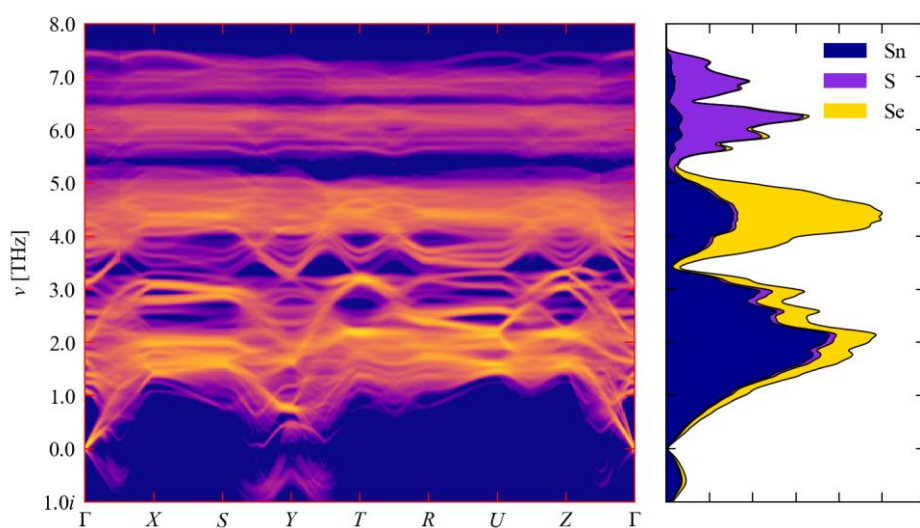


Figure S7 Simulated phonon spectra of a *Pnma* $\text{SnS}_{0.375}\text{Se}_{0.625}$ solid solution. The left-hand panel shows the phonon dispersion unfolded back to a *Pnma* parent structure. The right-hand panel shows the density of states $g(\nu)$ (DoS) as a stacked area plot with the projections onto Sn (blue), S (purple) and Se atoms (yellow). The averaging over structures in the solid-solution model was performed based on a formation temperature T_F of 900 K.

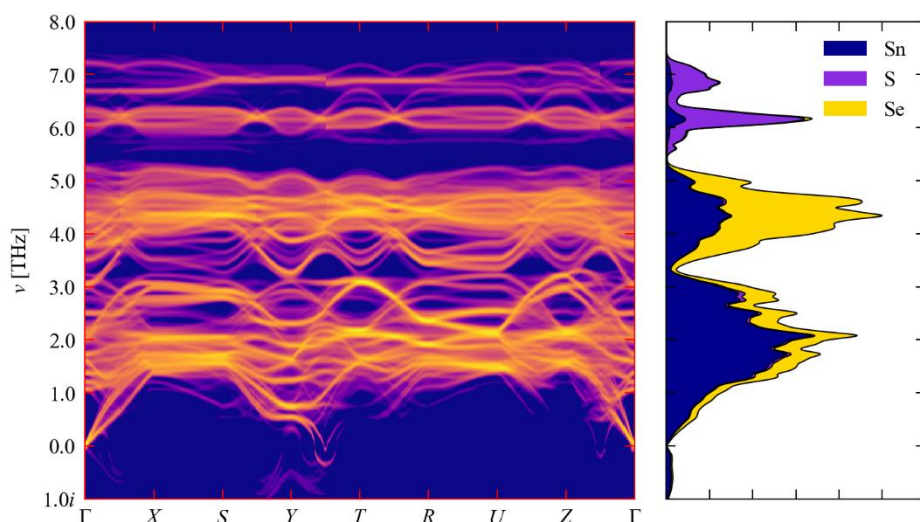


Figure S8 Simulated phonon spectra of a *Pnma* $\text{SnS}_{0.25}\text{Se}_{0.75}$ solid solution. The left-hand panel shows the phonon dispersion unfolded back to a *Pnma* parent structure. The right-hand panel shows the density of states $g(\nu)$ (DoS) as a stacked area plot with the projections onto Sn (blue), S (purple) and Se atoms (yellow). The averaging over structures in the solid-solution model was performed based on a formation temperature T_F of 900 K.

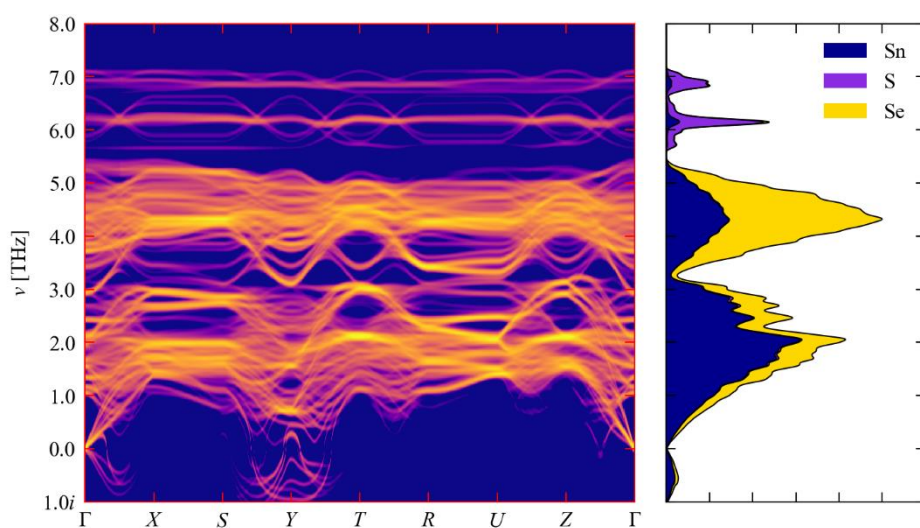


Figure S9 Simulated phonon spectra of a *Pnma* $\text{SnS}_{0.125}\text{Se}_{0.875}$ solid solution. The left-hand panel shows the phonon dispersion unfolded back to a *Pnma* parent structure. The right-hand panel shows the density of states $g(\nu)$ (DoS) as a stacked area plot with the projections onto Sn (blue), S (purple) and Se atoms (yellow). The averaging over structures in the solid-solution model was performed based on a formation temperature T_F of 900 K.

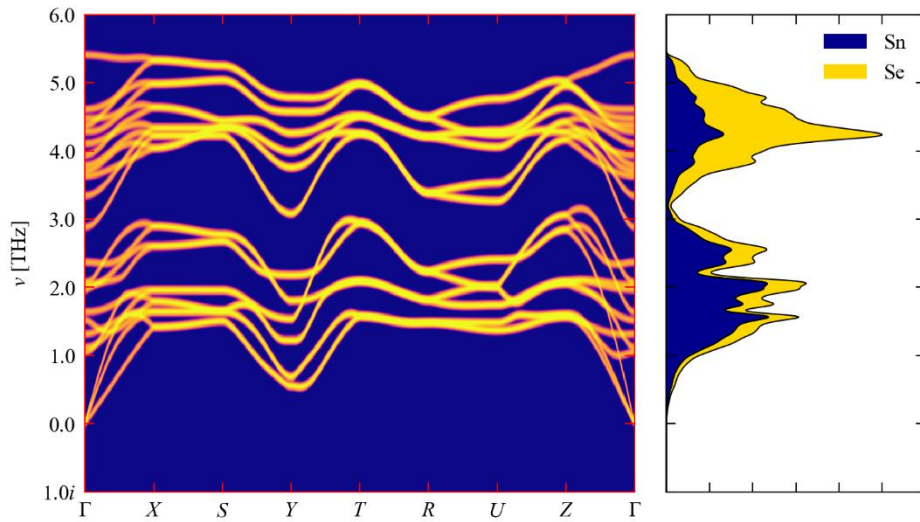


Figure S10 Simulated phonon spectra of *Pnma* SnSe. The left-hand panel shows the phonon dispersion and the right-hand panel shows the density of states $g(\nu)$ (DoS) as a stacked area plot with the projections onto Sn (blue) and Se atoms (yellow).

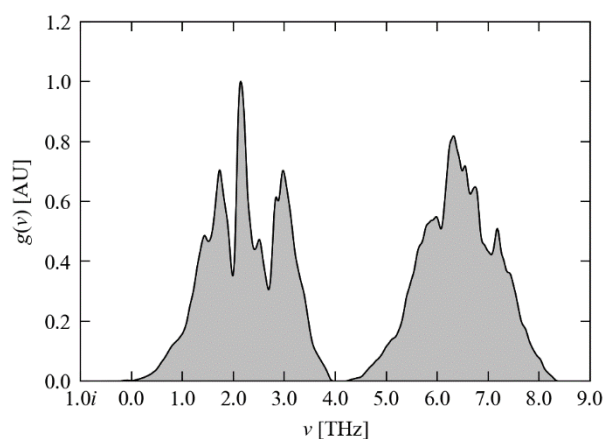


Figure S11 Simulated phonon density of states of *Pnma* SnS. The DoS was evaluated by interpolating the phonon frequencies onto a regular Γ -centred \mathbf{q} -point grid with $24 \times 16 \times 24$ subdivisions and using Gaussian smearing with a width $\sigma = 0.032$ THz (FWHM ~ 2.5 cm^{-1}) to integrate the Brillouin zone.

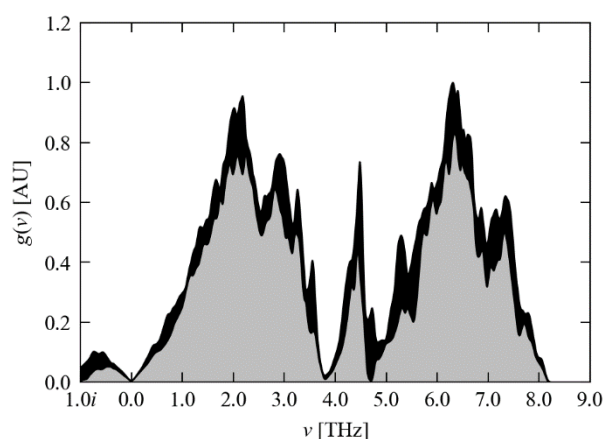


Figure S12 Simulated phonon density of states of a *Pnma* $\text{Sn}_{0.875}\text{Se}_{0.125}$ solid solution. The grey curve shows the averaged DoS and the shaded black region indicates \pm one weighted standard deviation. The DoS was evaluated by interpolating the phonon frequencies onto a regular Γ -centred \mathbf{q} -point grid with $24 \times 16 \times 24$ subdivisions and using Gaussian smearing with a width $\sigma = 0.032$ THz (FWHM ~ 2.5 cm^{-1}) to integrate the Brillouin zone. The averaging over structures in the solid-solution model was performed based on a formation temperature T_F of 900 K.

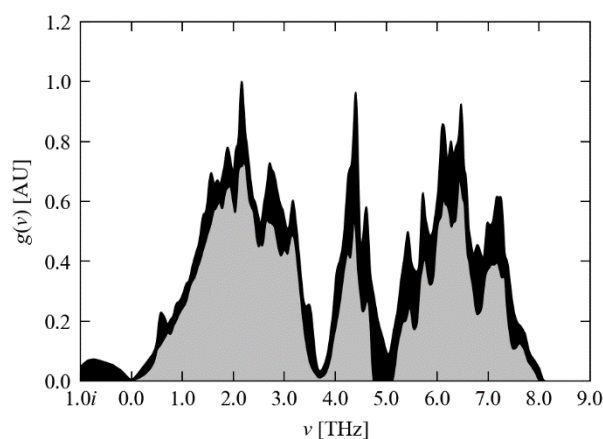


Figure S13 Simulated phonon density of states of a *Pnma* $\text{SnS}_{0.75}\text{Se}_{0.25}$ solid solution. The grey curve shows the averaged DoS and the shaded black region indicates \pm one weighted standard deviation. The DoS was evaluated by interpolating the phonon frequencies onto a regular Γ -centred \mathbf{q} -point grid with $24 \times 16 \times 24$ subdivisions and using Gaussian smearing with a width $\sigma = 0.032$ THz (FWHM ~ 2.5 cm^{-1}) to integrate the Brillouin zone. The averaging over structures in the solid-solution model was performed based on a formation temperature T_F of 900 K.

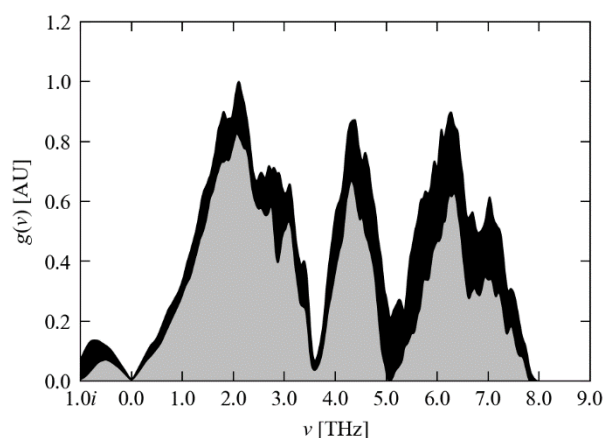


Figure S14 Simulated phonon density of states of a *Pnma* $\text{SnS}_{0.625}\text{Se}_{0.375}$ solid solution. The grey curve shows the averaged DoS and the shaded black region indicates \pm one weighted standard deviation. The DoS was calculated by interpolating the phonon frequencies onto a regular Γ -centred \mathbf{q} -point grid with $24 \times 16 \times 24$ subdivisions and using Gaussian smearing with a width $\sigma = 0.032$ THz (FWHM ~ 2.5 cm^{-1}) to integrate the Brillouin zone. The averaging over structures in the solid-solution model was performed based on a formation temperature T_F of 900 K.

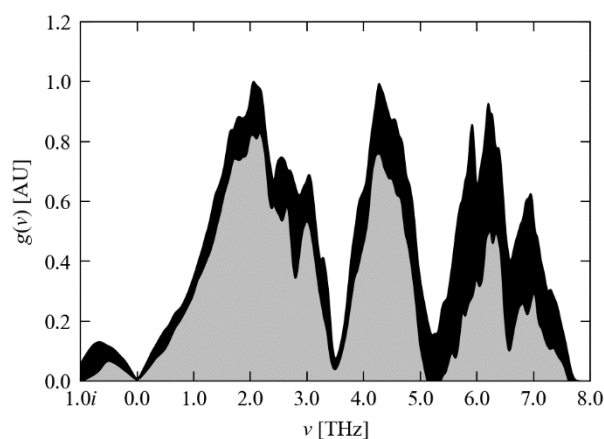


Figure S15 Simulated phonon density of states of a *Pnma* $\text{SnS}_{0.5}\text{Se}_{0.5}$ solid solution. The grey curve shows the averaged DoS and the shaded black region indicates \pm one weighted standard deviation. The DoS was evaluated by interpolating the phonon frequencies onto a regular Γ -centred \mathbf{q} -point grid with $24 \times 16 \times 24$ subdivisions and using Gaussian smearing with a width $\sigma = 0.032$ THz (FWHM ~ 2.5 cm^{-1}) to integrate the Brillouin zone. The averaging over structures in the solid-solution model was performed based on a formation temperature T_F of 900 K.

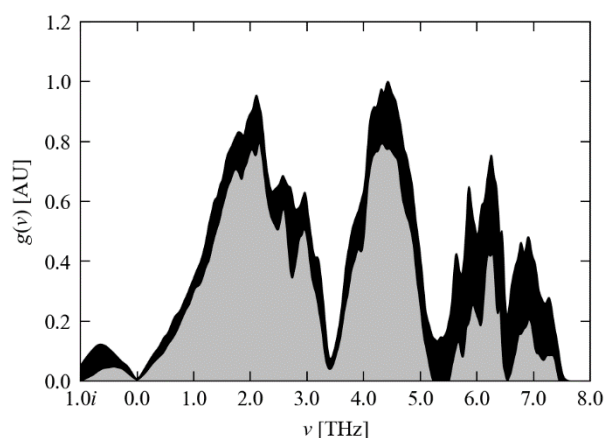


Figure S16 Simulated phonon density of states of a *Pnma* $\text{SnS}_{0.375}\text{Se}_{0.625}$ solid solution. The grey curve shows the averaged DoS and the shaded black region indicates \pm one weighted standard deviation. The DoS was evaluated by interpolating the phonon frequencies onto a regular Γ -centred \mathbf{q} -point grid with $24 \times 16 \times 24$ subdivisions and using Gaussian smearing with a width $\sigma = 0.032$ THz (FWHM ~ 2.5 cm^{-1}) to integrate the Brillouin zone. The averaging over structures in the solid-solution model was performed based on a formation temperature T_F of 900 K.

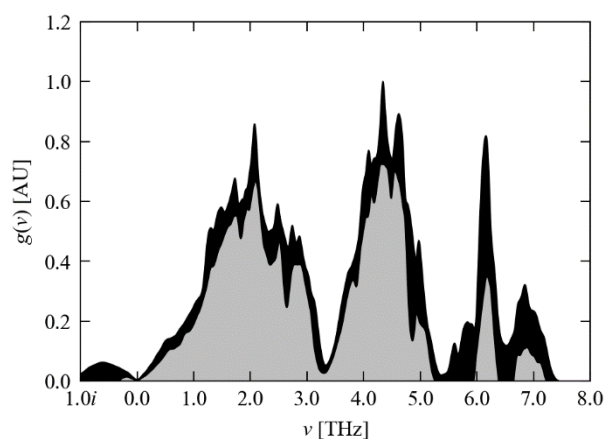


Figure S17 Simulated phonon density of states of a *Pnma* $\text{SnS}_{0.25}\text{Se}_{0.75}$ solid solution. The grey curve shows the averaged DoS and the shaded black region indicates \pm one weighted standard deviation. The DoS was evaluated by interpolating the phonon frequencies onto a regular Γ -centred \mathbf{q} -point grid with $24 \times 16 \times 24$ subdivisions and using Gaussian smearing with a width $\sigma = 0.032$ THz (FWHM ~ 2.5 cm^{-1}) to integrate the Brillouin zone. The averaging over structures in the solid-solution model was performed based on a formation temperature T_F of 900 K.

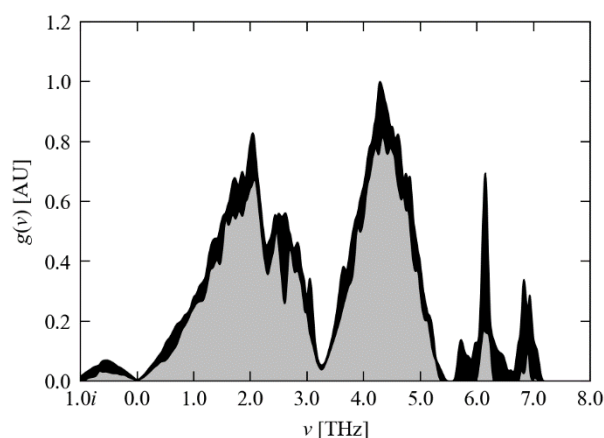


Figure S18 Simulated phonon density of states of a *Pnma* $\text{SnS}_{0.125}\text{Se}_{0.875}$ solid solution. The grey curve shows the averaged DoS and the shaded black region indicates \pm one weighted standard deviation. The DoS was evaluated by interpolating the phonon frequencies onto a regular Γ -centred \mathbf{q} -point grid with $24 \times 16 \times 24$ subdivisions and using Gaussian smearing with a width $\sigma = 0.032$ THz (FWHM ~ 2.5 cm^{-1}) to integrate the Brillouin zone. The averaging over structures in the solid-solution model was performed based on a formation temperature T_F of 900 K.

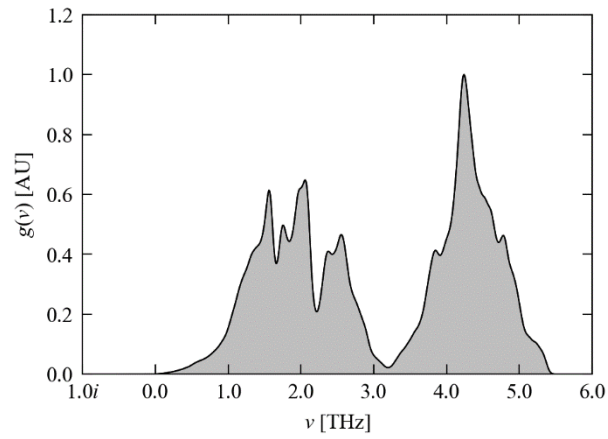


Figure S19 Simulated phonon density of states of *Pnma* SnSe. The DoS was evaluated by interpolating the phonon frequencies onto a regular Γ -centred \mathbf{q} -point grid with $24 \times 16 \times 24$ subdivisions and using Gaussian smearing with a width $\sigma = 0.032$ THz (FWHM ~ 2.5 cm^{-1}) to integrate the Brillouin zone.

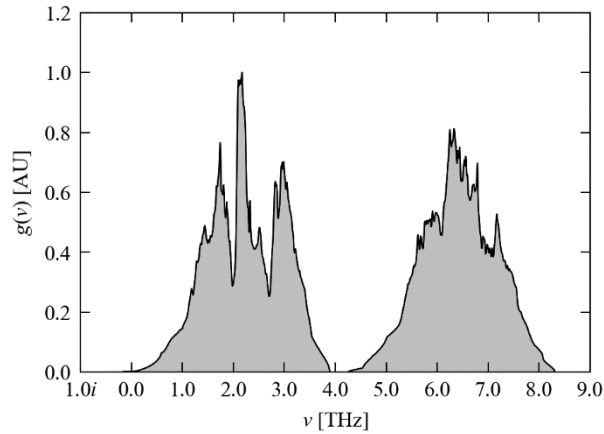


Figure S20 Simulated phonon density of states of *Pnma* SnS. The DoS was evaluated by interpolating the phonon frequencies onto a regular Γ -centred \mathbf{q} -point grid with $36 \times 24 \times 36$ subdivisions and using the linear tetrahedron method to integrate the Brillouin zone.

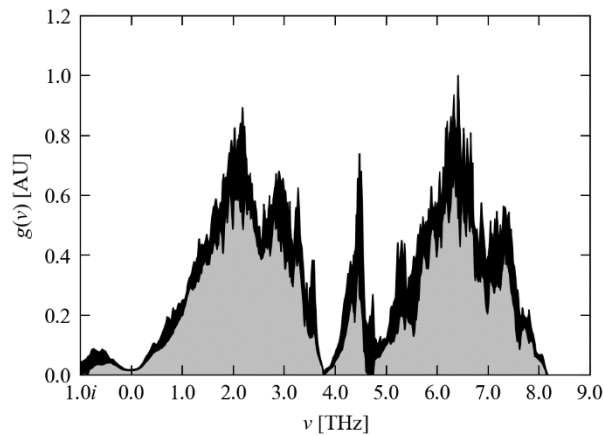


Figure S21 Simulated phonon density of states of a *Pnma* $\text{Sn}_{0.875}\text{Se}_{0.125}$ solid solution. The grey curve shows the averaged DoS and the shaded black region indicates \pm one weighted standard deviation. The DoS was evaluated by interpolating the phonon frequencies onto a regular Γ -centred \mathbf{q} -point grid with $36 \times 24 \times 36$ subdivisions and using the linear tetrahedron method to integrate the Brillouin zone. The averaging over structures in the solid-solution model was performed based on a formation temperature T_F of 900 K.

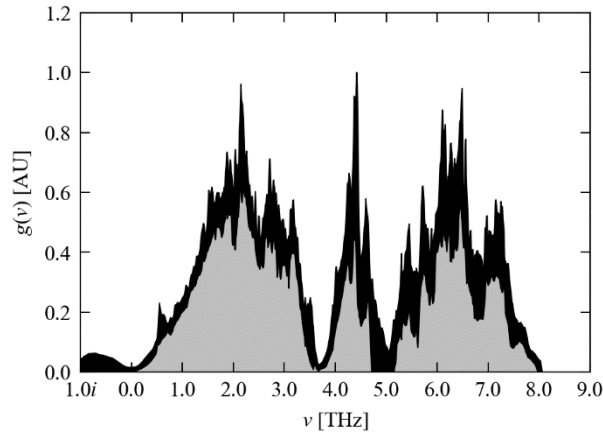


Figure S22 Simulated phonon density of states of a *Pnma* $\text{SnS}_{0.75}\text{Se}_{0.25}$ solid solution. The grey curve shows the averaged DoS and the shaded black region indicates \pm one weighted standard deviation. The DoS was evaluated by interpolating the phonon frequencies onto a regular Γ -centred \mathbf{q} -point grid with $36 \times 24 \times 36$ subdivisions and using the linear tetrahedron method to integrate the Brillouin zone. The averaging over structures in the solid-solution model was performed based on a formation temperature T_{F} of 900 K.

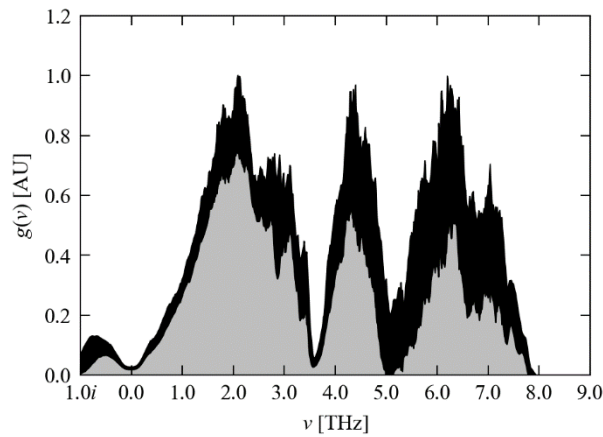


Figure S23 Simulated phonon density of states of a *Pnma* $\text{SnS}_{0.625}\text{Se}_{0.375}$ solid solution. The grey curve shows the averaged DoS and the shaded black region indicates \pm one weighted standard deviation. The DoS was evaluated by interpolating the phonon frequencies onto a regular Γ -centred \mathbf{q} -point grid with $36 \times 24 \times 36$ subdivisions and using the linear tetrahedron method to integrate the Brillouin zone. The averaging over structures in the solid-solution model was performed based on a formation temperature T_{F} of 900 K.

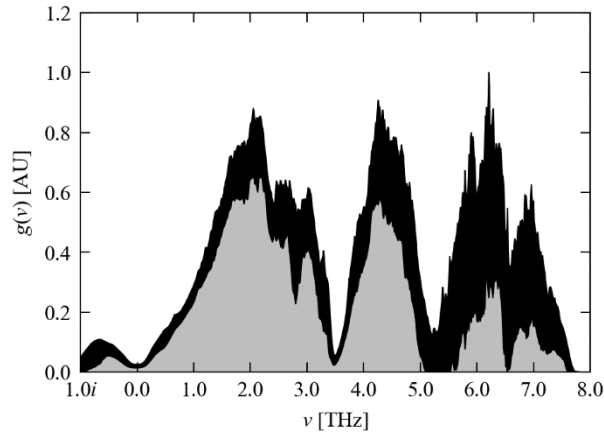


Figure S24 Simulated phonon density of states of a *Pnma* $\text{SnS}_{0.5}\text{Se}_{0.5}$ solid solution. The grey curve shows the averaged DoS and the shaded black region indicates \pm one weighted standard deviation. The DoS was evaluated by interpolating the phonon frequencies onto a regular Γ -centred \mathbf{q} -point grid with $36 \times 24 \times 36$ subdivisions and using the linear tetrahedron method to integrate the Brillouin zone. The averaging over structures in the solid-solution model was performed based on a formation temperature T_{F} of 900 K.

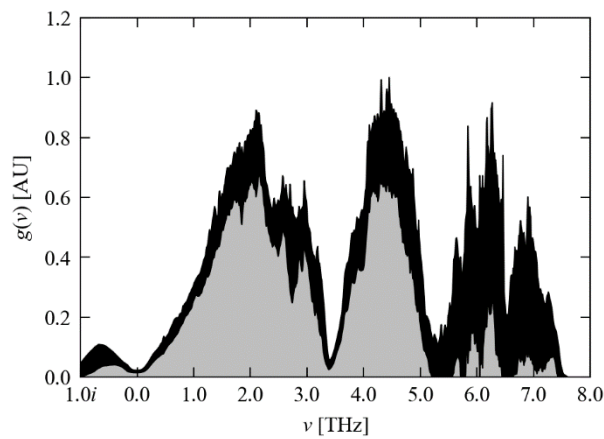


Figure S25 Simulated phonon density of states of a *Pnma* $\text{SnS}_{0.375}\text{Se}_{0.625}$ solid solution. The grey curve shows the averaged DoS and the shaded black region indicates \pm one weighted standard deviation. The DoS was evaluated by interpolating the phonon frequencies onto a regular Γ -centred \mathbf{q} -point grid with $36 \times 24 \times 36$ subdivisions and using the linear tetrahedron method to integrate the Brillouin zone. The averaging over structures in the solid-solution model was performed based on a formation temperature T_{F} of 900 K.

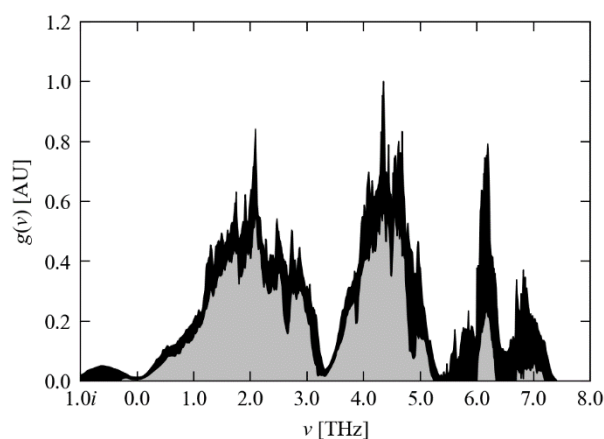


Figure S26 Simulated phonon density of states of a *Pnma* $\text{SnS}_{0.25}\text{Se}_{0.75}$ solid solution. The grey curve shows the averaged DoS and the shaded black region indicates \pm one weighted standard deviation. The DoS was evaluated by interpolating the phonon frequencies onto a regular Γ -centred \mathbf{q} -point grid with $36 \times 24 \times 36$ subdivisions and using the linear tetrahedron method to integrate the Brillouin zone. The averaging over structures in the solid-solution model was performed based on a formation temperature T_{F} of 900 K.

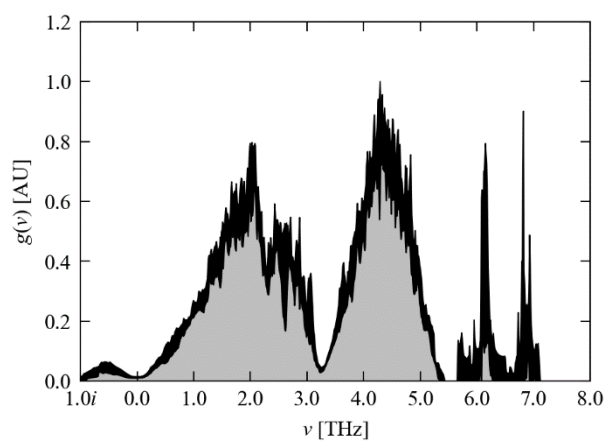


Figure S27 Simulated phonon density of states of a *Pnma* $\text{SnS}_{0.125}\text{Se}_{0.875}$ solid solution. The grey curve shows the averaged DoS and the shaded black region indicates \pm one weighted standard deviation. The DoS was evaluated by interpolating the phonon frequencies onto a regular Γ -centred \mathbf{q} -point grid with $36 \times 24 \times 36$ subdivisions and using the linear tetrahedron method to integrate the Brillouin zone. The averaging over structures in the solid-solution model was performed based on a formation temperature T_{F} of 900 K.

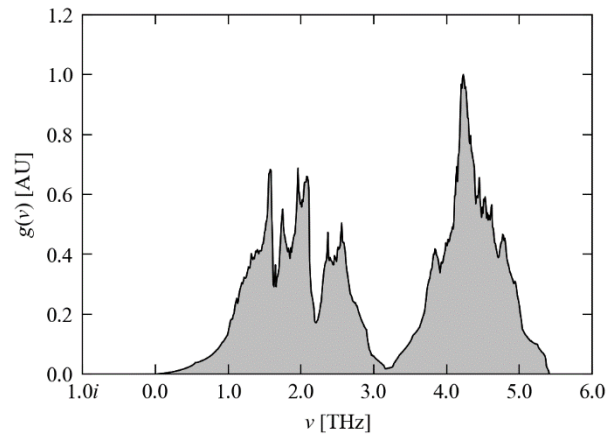


Figure S28 Simulated phonon density of states of *Pnma* SnSe. The DoS was evaluated by interpolating the phonon frequencies onto a regular Γ -centred \mathbf{q} -point grid with $36 \times 24 \times 36$ subdivisions and using the linear tetrahedron method to integrate the Brillouin zone.

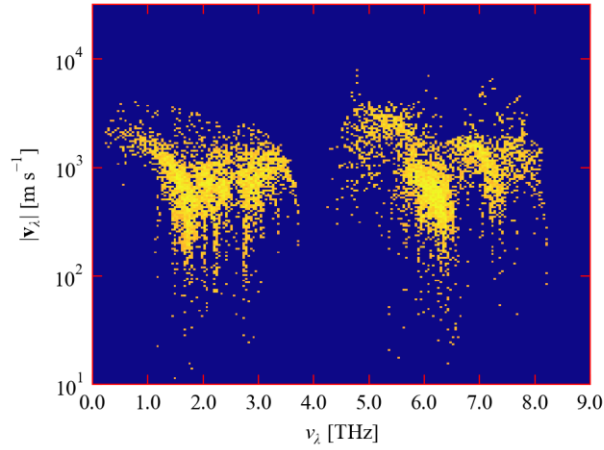


Figure S29 Simulated frequency spectrum of the group velocity norms $|v_\lambda|$ in *Pnma* SnS. The colour scale indicates the density of modes and runs from red (low density) to yellow (high density). As in Fig. 5 in the text, this data was taken from the previous calculation in Ref. [1].

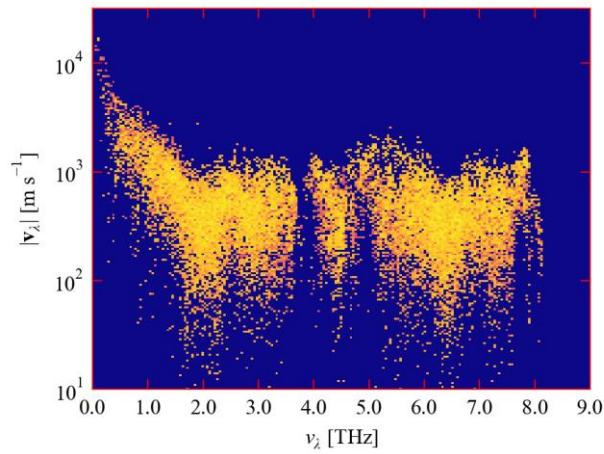


Figure S30 Simulated frequency spectrum of the group velocity norms $|v_\lambda|$ in a *Pnma* SnS_{0.875}Se_{0.125} solid solution. The colour scale indicates the density of modes and runs from red (low density) to yellow (high density). The averaging over structures in the solid-solution model was performed based on a formation temperature T_F of 900 K.

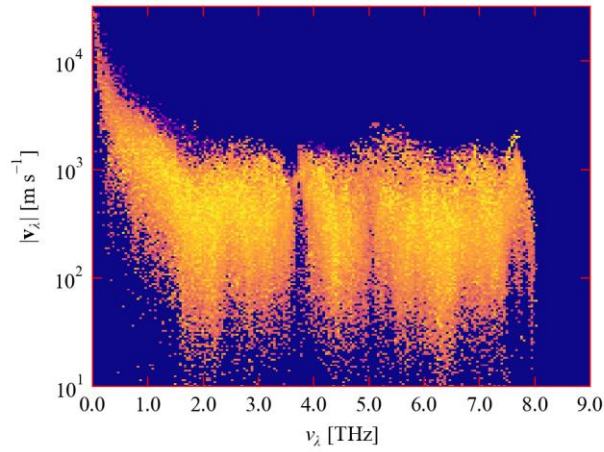


Figure S31 Simulated frequency spectrum of the group velocity norms $|v_\lambda|$ in a *Pnma* $\text{SnS}_{0.75}\text{Se}_{0.25}$ solid solution. The colour scale indicates the density of modes and runs from red (low density) to yellow (high density). The averaging over structures in the solid-solution model was performed based on a formation temperature T_F of 900 K.

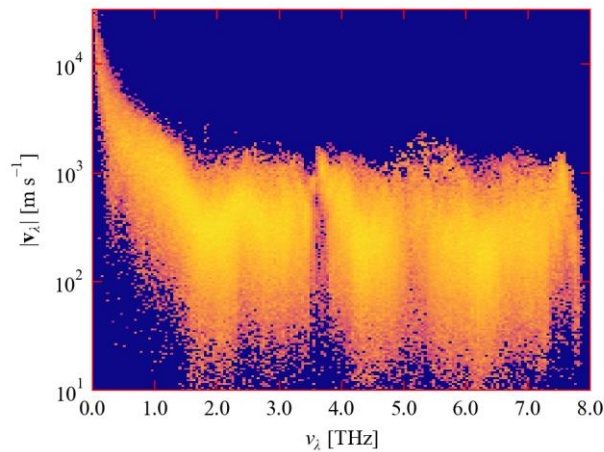


Figure S32 Simulated frequency spectrum of the group velocity norms $|v_\lambda|$ in a *Pnma* $\text{SnS}_{0.625}\text{Se}_{0.375}$ solid solution. The colour scale indicates the density of modes and runs from red (low density) to yellow (high density). The averaging over structures in the solid-solution model was performed based on a formation temperature T_F of 900 K.

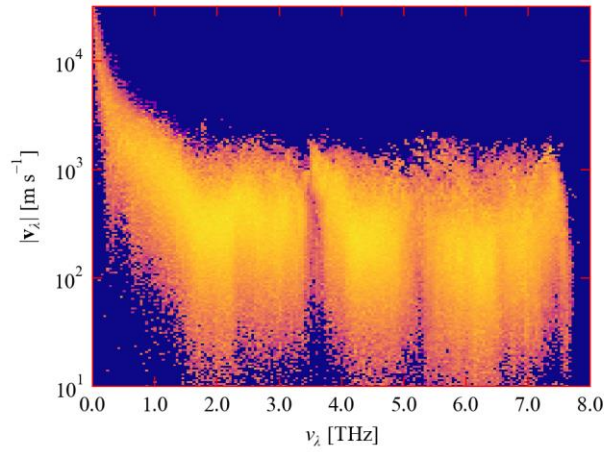


Figure S33 Simulated frequency spectrum of the group velocity norms $|v_\lambda|$ in a *Pnma* $\text{SnS}_{0.5}\text{Se}_{0.5}$ solid solution. The colour scale indicates the density of modes and runs from red (low density) to yellow (high density). The averaging over structures in the solid-solution model was performed based on a formation temperature T_F of 900 K.

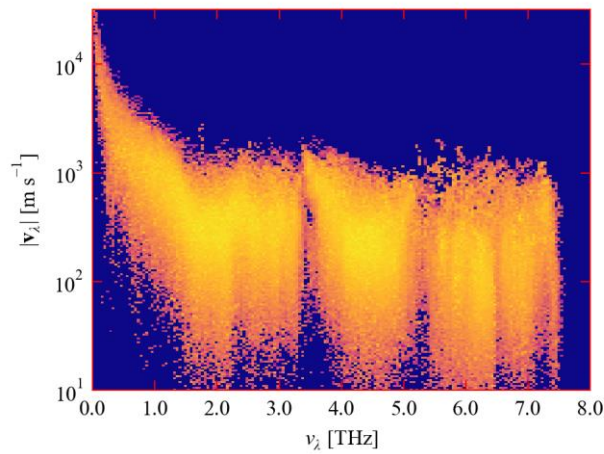


Figure S34 Simulated frequency spectrum of the group velocity norms $|v_\lambda|$ in a *Pnma* $\text{SnS}_{0.375}\text{Se}_{0.625}$ solid solution. The colour scale indicates the density of modes and runs from red (low density) to yellow (high density). The averaging over structures in the solid-solution model was performed based on a formation temperature T_F of 900 K.

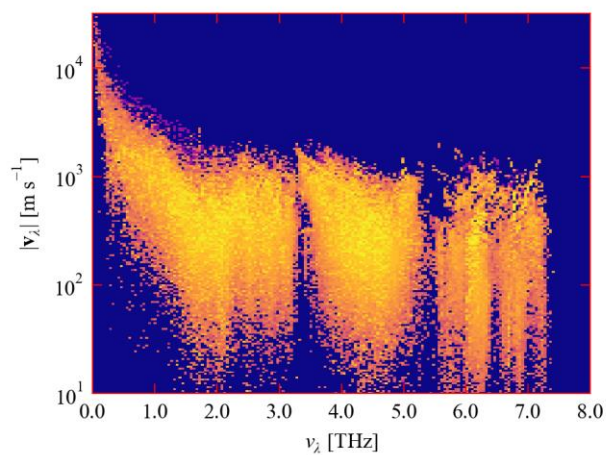


Figure S35 Simulated frequency spectrum of the group velocity norms $|v_\lambda|$ in a *Pnma* $\text{SnS}_{0.25}\text{Se}_{0.75}$ solid solution. The colour scale indicates the density of modes and runs from red (low density) to yellow (high density). The averaging over structures in the solid-solution model was performed based on a formation temperature T_F of 900 K.

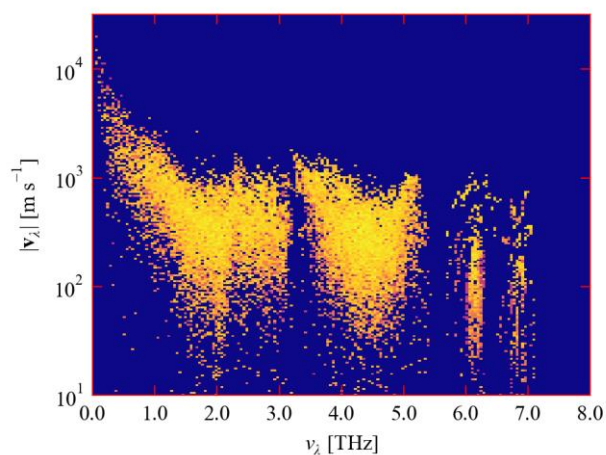


Figure S36 Simulated frequency spectrum of the group velocities in a *Pnma* $\text{SnS}_{0.125}\text{Se}_{0.875}$ solid solution. The colour scale indicates the density of modes and runs from red (low density) to yellow (high density). The averaging over structures in the solid-solution model was performed based on a formation temperature T_F of 900 K.

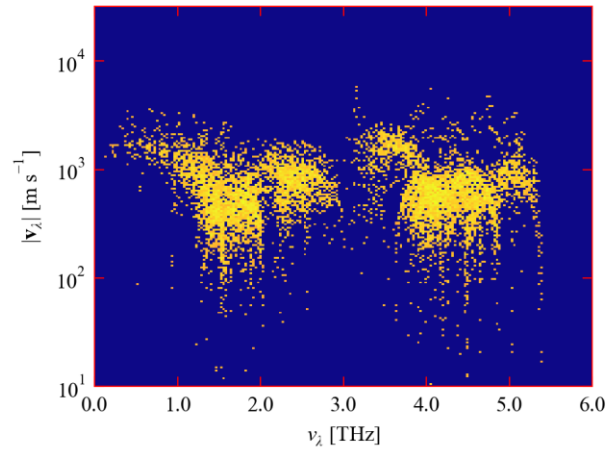


Figure S37 Simulated frequency spectrum of the group velocity norms $|v_\lambda|$ in *Pnma* SnSe. The colour scale indicates the density of modes and runs from red (low density) to yellow (high density). As in Fig. 5 in the text, this data was taken from the previous calculation in Ref. [2].

- [1] Skelton J M, Burton L A, Jackson A J, Oba F, Parker S C and Walsh A 2017 Lattice dynamics of the tin sulphides SnS₂, SnS and Sn₂S₃: Vibrational spectra and thermal transport *Phys. Chem. Chem. Phys.* **19** 12452–65
- [2] Skelton J M, Burton L A, Parker S C, Walsh A, Kim C-E, Soon A, Buckeridge J, Sokol A A, Catlow C R A, Togo A and Tanaka I 2016 Anharmonicity in the High-Temperature *Cmcm* Phase of SnSe: Soft Modes and Three-Phonon Interactions *Phys. Rev. Lett.* **117** 075502